BBA - Gene Regulatory Mechanisms 1863 (2020) 194515

Contents lists available at ScienceDirect

BBA - Gene Regulatory Mechanisms

journal homepage: www.elsevier.com/locate/bbagrm

Dissecting the *in vivo* dynamics of transcription locking due to positive supercoiling buildup

Cristina S.D. Palma, Vinodh Kandavalli, Mohamed N.M. Bahrudeen, Marco Minoia, Vatsala Chauhan, Suchintak Dash, Andre S. Ribeiro*

Laboratory of Biosystem Dynamics, BioMediTech, Faculty of Medicine and Health Technology, Tampere University, 33101 Tampere, Finland

ARTICLE INFO

Keywords:
Single-RNA production dynamics
Positive supercoiling buildup
LineWeaver-Burk plots
Transcription locking kinetics

ABSTRACT

Positive supercoiling buildup (PSB) is a pervasive phenomenon in the transcriptional programs of *Escherichia coli*. After finding a range of Gyrase concentrations where the inverse of the transcription rate of a chromosome-integrated gene changes linearly with the inverse of Gyrase concentration, we apply a LineWeaver-Burk plot to dissect the expected *in vivo* transcription rate in absence of PSB. We validate the estimation by time-lapse microscopy of single-RNA production kinetics of the same gene when single-copy plasmid-borne, shown to be impervious to Gyrase inhibition. Next, we estimate the fraction of time in locked states and number of transcription events prior to locking, which we validate by measurements under Gyrase inhibition. Replacing the gene of interest by one with slower transcription rate decreases the fraction of time in locked states due to PSB. Finally, we combine data from both constructs to infer a range of possible transcription initiation locking kinetics in a chromosomal location, obtainable by tuning the transcription rate. We validate with measurements of transcription activity at different induction levels. This strategy for dissecting transcription initiation locking kinetics due to PSB can contribute to resolve the transcriptional programs of *E. coli* and in the engineering of synthetic genetic circuits.

1. Introduction

Transcription in *Escherichia coli* generates positive supercoiling ahead of the RNAP and negative supercoiling behind it ([11,46,51]; [87,95,99]). Discrete, topologically constrained segments along the DNA cause this process to generate local supercoiling buildup [31,33,41,70,77]. Evidence suggests that this torsional stress can affect gene activity [2,96].

E. coli has (at least) two proteins to resolve torsional stress. Namely, Gyrase removes positive supercoils [9,15,46] while Topoisomerase I removes negative supercoils [9,15,22,35,46,90]. Interestingly, in normal conditions, Topoisomerase I removes the negative supercoils at sufficient speed for R loops to not emerge, which is essential for cell survival [16]. This is made possible by the existence of a direct physical interaction between the RNAP and Topoisomerase I, allowing the latter to remove the negative supercoils, as soon as they form [7]. Contrarily to this, the removal of positive supercoils is not as efficient (being an ATP-dependent reaction likely contributes to this [77]), in the sense that positive supercoiling buildup (PSB) is commonly observed, particularly in highly active operons [17,28]. In support, measurements have shown that Topoisomerase I can relax plasmid DNA ~6 times faster than Topoisomerase IV [97], which has the same catalytic rate as Gyrase [84].

As positive supercoils accumulate, elongation slows down and, eventually, there are transient halts in transcription initiation [9,73]. These halts in initiation tangibly decrease RNA production rates and increase transcriptional noise [9,55,59]. Thus, dissection of the *in vivo* kinetics of transcription locking due to PSB is needed in order to dissect the transcriptional programs of *E. coli*.

A strategy was recently introduced for dissecting the *in vivo* kinetics of rate-limiting steps of active transcription initiation from *in vivo* measurements of individual RNA production events at different RNA polymerase (RNAP) concentrations [48]. It uses a Lineweaver–Burk plot [44] to infer the time-length of events *prior* and *after* commitment to open complex formation [58] from measurements of *in vivo*transcription rates at different RNAP concentrations ([RNAP]) [48]. This is possible due to the independence of the kinetics of the open complex formation from [RNAP], and because there is a range of values of [RNAP] for which the inverse of RNA production rate changes linearly with the inverse of [RNAP] [48].

* Corresponding author at: Tampere University, Arvo Ylpön katu 34, P.O. Box 100, 33014 Tampere, Finland.
E-mail address: andre.sanchesribeiro@tuni.fi (A.S. Ribeiro).

https://doi.org/10.1016/j.bbagrm.2020.194515
Received 14 June 2019; Received in revised form 7 February 2020; Accepted 20 February 2020
Available online 27 February 2020

Similarly, chromosomal RNA production rates (particularly of genes in highly transcribed operons) are expected to differ with Gyrase concentration, due to the existence of discrete topological constraints [9,69,70]. Thus, it should be possible to, from *in vivo* RNA production rates at different Gyrase concentrations, infer the kinetics of *in vivo* transcription locking due to PSB. For this, it must hold true that there is a range of conditions for which the inverse of the RNA production rate changes linearly with the inverse of Gyrase concentration.

Here we verify this hypothesis and then use this strategy to dissect the contribution of transcription initiation locking due to PSB on the kinetics of RNA production of a chromosome-integrated gene. We validate the estimation by time-lapse microscopy of single-RNA production kinetics of the same gene when single-copy plasmid-borne, shown to be impervious to Gyrase inhibition. Based on this, we estimate the fraction of time in locked states and the number of transcription events prior to locking, which we validate by measurements of RNA production under the inhibition of Gyrase activity by the addition of Novobiocin (see Section 2.3). Replacing our gene by a gene with a slower transcription rate, we show that changes in the *basal* transcription rate (expected rate of RNA production in the absence of effects from PSB) affect the contribution of locking due to PSB on *effective* transcription rates (measured rate of RNA production). Finally, we infer a range of possible transcription initiation locking kinetics in a chromosomal location, obtainable by tuning the basal transcription rate, and validate this inference using measurements of transcription activity at different induction levels.

2. Materials and methods

2.1. Strains and plasmids

We engineered two strains from *E. coli* BW25993 (*lacI^q hsdR514 ΔaraBAD$_{AH33}$ ΔrhaBAD$_{LD78}$*) [10]. In one strain, the target gene $P_{LacO3O1}$-mCherry-MS2-BS is integrated into a single-copy F-plasmid (~11 kbp), pBELOBAC11 (target plasmid). This plasmid is not known to form long-lasting bounds to the cell membrane and is originally responsible for the expression of transient DNA-binding proteins [27,32,60]. In the other strain this plasmid is absent and the same target gene, $P_{LacO3O1}$-mCherry-MS2-BS, is integrated into the lac locus of the genome using Red/ET recombination (Gene Bridges, Heidelberg, Germany) (Supplementary Figs. S1A and S1B). We found no significant differences in the growth rates of the two strains and the original strain.

$P_{LacO3O1}$, inducible by IPTG, was engineered from the *E. coli* native P_{Lac} by removing the O2 repressor binding site downstream of the transcription start site [62]. Thus, strong topological barriers are not expected to form when fully induced [21]. Also, both strains were transformed with the medium-copy reporter plasmid pZA25-GFP [61] (kind gift from Orna Amster-Choder, Hebrew University of Jerusalem, Israel), coding for the reporter MS2-GFP under the control of the P_{BAD} promoter. The strain with the target gene in a single-copy F-plasmid also contains the native Lac promoter in the chromosome. Thus, it has 4 LacI binding sites. The strain with the chromosome-integrated target gene only has 2 LacI binding sites, as the original Lac promoter was replaced by the target promoter, $LacO_3O_1$. However, as both strains overexpress LacI [10], effects of this difference are expected to be negligible.

Both target genes (plasmid and chromosome constructs) code for an RNA with an array of bindings sites (BS) for the modified viral coat protein MS2-GFP [25,67,68]. Due to the multiple BS in the target RNA and the strong binding affinity of each site [25], MS2-GFP tagged RNAs appear as bright spots soon after produced (Supplementary Figs. S2B and S2D). Their maximum fluorescence is reached rapidly (< 1 min) and have long half-lives (Supplementary Section I).

For overexpressing Gyrase, we constructed a plasmid (pZe11 P_{rham} gyrAB-*sfGFP*, with ampicillin resistance) with the *gyrA* and *gyrB* genes under the control of a Rhamnose promoter. These genes were arranged in a polycistronic manner, using their (identical) ribosome-binding site to maintain the physiological stoichiometry of the two subunits. We amplified the sfGFP using the primers: Forward: 5′CATATGAGCAAAG GAGAAGAACTTTT 3′, Reverse: 5′ CGGCCGTTTGTAGAGCTCATCCA TGC 3′ with restriction enzymes and cloned it after the *gyrAB* genes by digestion followed by ligation (Supplementary Fig. S3). We also constructed a plasmid without sfGFP, by digesting with the restriction enzymes *Nde*I and *Nae*I, followed by ligation, which was transferred to *E. coli* BW25993 with the $P_{LacO3O1}$-mCherry-MS2-BS integrated into a single-copy F-plasmid [27] and to *E. coli* BW25993 with the $P_{LacO3O1}$-mCherry-MS2-BS integrated in the chromosome. Finally, in another strain, we replaced the chromosome-integrated $P_{LacO3O1}$ by the native Lac promoter, followed by the same array of binding sites for MS2-GFP.

To access the intracellular levels of Gyrase A proteins, we used a strain with a gyrA gene endogenously tagged with the YFP coding sequence [85]. From the glycerol stock (-80 °C), cells were streaked on the LB agar plates and incubated at 37 °C overnight. From the plate, a single colony was picked, inoculated in an LB medium supplemented with the antibiotics, and incubated at 30 °C overnight with shaking at 250 RPM. Next, cells were diluted into fresh LB medium to an OD of 0.03 (Optical Density, 600 nm; Ultrospec 10, Amersham biosciences, UK) and grown at 37 °C with 250 RPM until it reaches to the mid-exponential phase (OD ~0.4–0.5).

2.2. Nucleoid visualization by DAPI staining

DAPI (4′,6-diamidino-2-phenylindole) stains nucleoids specifically with little or no cytoplasmic labelling. Gyrase induced and un-induced cells were grown at 37 °C and fixed with 3.7% formaldehyde in phosphate buffered saline (PBS, pH 7.4) for 30 min at room temperature, followed by washing with PBS to remove excess formaldehyde. The pellets were suspended in PBS, and DAPI (2 μg/ml) was added to the suspension. After incubating for 20 min in the dark, cells were centrifuged and washed twice with PBS to remove excess DAPI. Cells were then re-suspended in PBS and 3 μl of these cells were placed on a 1% agarose gel pad for microscopy.

2.3. Growth conditions and induction of the reporter and target gene

From a -80 °C glycerol stock, cells were placed in LB medium agar plates with 34 μg/ml Chloramphenicol and 35 μg/ml Kanamycin (Sigma-Aldrich, USA) and incubated overnight at 37 °C (Innova® 40 incubator, New Brunswick Scientific, USA). Cells were cultured in LB medium from single colonies on LB agar plates with the appropriate concentration of antibiotics and incubated overnight at optimal temperature at 250 rpm with aeration. These cultures were diluted to an optical density (OD_{600}) of 0.05 in fresh M9 medium, with a culture volume of 20 ml supplemented with the appropriate antibiotics and 0.4% of Glycerol (Sigma-Aldrich, USA), and incubated for 3 h with a 250 rpm agitation until an OD_{600} of ~ 0.3. Next, to induce MS2-GFP expression, 0.4% of L-Arabinose (Sigma-Aldrich, USA) was added and cells were incubated for another 45 min for sufficient MS2-GFP to accumulate for detecting target RNAs [26]. Next, the target gene was induced by IPTG (Sigma-Aldrich, USA) and cells were incubated for 1 h, prior to image acquisition or RT-PCR. To obtain induction curves of target genes (under the control of $P_{LacO3O1}$ and P_{Lac}), 0, 50, 100, 250, 500 and 1000 μM IPTG was added (Supplementary Fig. S4A). Unless stated otherwise, the target genes are always fully induced by 1000 μM IPTG.

We also performed measurements when inactivating and when overexpressing Gyrase. To inactive gyrase, we follow the protocol above, but when MS2-GFP expression is induced, we further added Novobiocin (100 μg/ml) [22]. Since all strains used here contain the gene *acrA*, Novobiocin at this concentration is not expected to affect cell division rate [50]. We verified this by measuring growth rates by OD_{600} for varying Novobiocin concentration (0, 25, 50, 75, 100, 200,

400, 500 ng/μl). The measurements show that growth rates to not differ significantly at 100 μg/ml or lower (Supplementary Fig. S5A). We further verified that Novobiocin does not affect morphology at these concentrations (see Section 3.6).

To overexpress Gyrase, we use Rhamnose (see previous Section) [93]. We follow the protocol above but, when inducing MS2-GFP expression, we also added Rhamnose. When applicable, Gyrase and RNAP concentrations were measured 1 h after adding Rhamnose. Gyrase overexpression did not affect bacteria growth (Supplementary Fig. S5B) nor morphology (see Section 3.2).

2.4. RT-PCR

One hour after inducing the target gene, cells were fixed by RNAProtect bacteria reagent (Qiagen, Germany), followed by enzymatic lysis with Tris-EDTA Lysozyme (15 mg/ml) buffer (pH 8.3). From the lysates, the RNA content was isolated using RNeasy purification kit (Qiagen) as per the manufacturer instructions. The RNA was then separated by electrophoresis using 1% agarose gel stained with SYBR® Safe DNA Gel Stain (Thermo Scientific, USA). The RNA was intact, with clear bands for the 16S and 23S ribosomal RNA. The RNA yield (~2 μg/μl) and absorbance ratios A260/A280 nm and A260/A230 nm were measured by a Nanovue Plus Spectrophotometer (GE Healthcare Life Sciences, USA). The ratio (2.0–2.1) indicates highly purified RNA. To remove DNA contamination, samples were treated with DNaseI (Thermo Scientific, USA) as per the manufacturer instructions. The cDNA was synthesized from 1 μg of RNA using iScript Reverse Transcription Supermix (Biorad, USA) as per the manufacturer instructions. cDNA samples (10 ng/μl) were mixed with qPCR master mix with iQ SYBR Green supermix (Biorad, USA) with primers (200 nM) for target and reference genes. 16S rRNA was used as reference. Primers set for target mRNA (mCherry) and reference (16S rRNA) genes were: mCherry (Forward: 5' CACCTACAAGGCCAAGAAGC 3′, Reverse: 5′ TGGTGTAGTCCTCGTTGTGG 3′), 16S rRNA (Forward: 5' CGTCAGCTC GTGTTGTGAA 3′, Reverse: 5′ GGACCGCTGGCAACAAAG 3′). To determine fold changes in mRNA Gyrase, cells were grown in M9 media supplemented with different Rhamnose concentrations. For the Gyrase mRNA (GyrA) gene the primer set was: Forward: 5' GGATTATGCGAT GTCGGTTCAT 3′, Reverse: 5′ CTAGCACAGTATCTGGCGGCT 3′. For mRNA sfGFP the primer set used was: Forward: 5′ GGAAAACTACCTG TTCCGTGGC 3′, Reverse: 5' ACATAACCTTCGGGCATGGCAC 3′. Experiments were performed by a Biorad MiniOpticon Real Time PCR System (Biorad, USA). The thermal cycling protocol was 40 cycles of 95 °C for 10 s, 52 °C for 30 s, and 72 °C for 30 s, with the fluorescence being read after each cycle. For each condition, we performed 3 biological replicates. qPCR efficiencies of these reactions were > 95%. No-RT and no-template controls were used to crosscheck non-specific signals and contamination. Cq values from the CFX ManagerTM Software were used to calculate fold changes in the target gene (normalized to the reference gene) and standard error, using Livak's $2^{-\Delta\Delta CT}$ method (40). RT-qPCR results are presented in Table S1.

2.5. Flow cytometry

To measure single cell Gyrase-GFP expression levels, cells were grown as described in Section 2.1. Upon reaching mid exponential phase, cells were diluted 1:1000 into 1 ml PBS vortexed for 10 s and 50,000 cells were tested in each run. Data was collected by an ACEA NovoCyte Flow Cytometer (ACEA Biosciences Inc., San Diego USA) using a blue laser (488 nm) for excitation and the fluorescein isothiocyanate detection channel (FITC) (530/30 nm filter) for emission, at a flow rate of 14 μl/min and a core diameter of 7.7 μM. A PMT voltage of 417 was used for FITC. To avoid background signal from particles smaller than bacteria, the detection threshold was set to 5000 in FSC-H analyses. We set the fraction of the cells used in the analysis (α) to 0.55, to remove any undesired data points from debris, cell doublets etc. Reducing α further did not change the results.

2.6. Western blot

Cells were grown as above until reaching an OD_{600} of 0.6. Pelleted cells were lysed with B-PER bacterial protein extraction reagent (Thermo scientific) and proteins were extracted. Protein samples were diluted with 4× laemmli sample loading buffer and boiled for 5 mins at 95 °C. 30 μg of proteins were loaded on the 4–20% TGX stain free pre cast gel (Biorad) and separated by electrophoresis. Proteins were then transferred to PVDF membrane using Trans-Blot Turbo transfer system (Biorad). The membrane was blocked with 5% non-fat milk and incubated with primary RpoC antibody 1:2000 dilutions (Biolegend) overnight at 4 °C and followed by HRP-secondary antibodies 1:5000 dilutions (Sigma Aldrich) for 1 h at room temperature. For band detection, the membrane was treated with a chemiluminescence reagent (Biorad). Images were acquired by the Chemidoc XRS system (Biorad). Band quantification was done using Image lab software (version 5.2.1). For each condition, we performed 3 biological replicates.

2.7. Microscopy and image analysis

Cells were grown as above, and pelleted and re-suspended in ~100 μl of the remaining media. Prior to imaging, cells were placed on a 2% agarose gel pad of M9 medium and kept in between the microscope slide and a coverslip. Cells were visualized by a Nikon Eclipse (Ti-E) inverted microscope with a 100× Apo TIRF (1.49 NA, oil) objective. Confocal images were taken by a C2+ (Nikon) confocal laser-scanning system with a pinhole size of 1.2 AU. In confocal images, the size of a pixel corresponds to 0.062 μm using a scan area resolution of 2048 × 2048 pixels. MS2-GFP-RNA spots and GyrA-YFP regions were visualized by a 488 nm laser and a 514/30 emission filter, while DAPI-stained nucleoids were visualized by a 405 nm laser and a 447/60 emission filter.

Phase contrast images were taken by an external phase contrast system and DS-Fi2 CCD camera (Nikon). Image sizes were 2560 × 1920 pixels, each pixel corresponding to 0.048 μm. Phase contrast and confocal images were taken simultaneously by Nis-Elements software (Nikon).

From phase contrast images, we segmented cells with the software iCellFusion [78] (Supplementary Figs. S2A and S2C). Errors were manually corrected. Next, phase-contrast and corresponding fluorescence images were aligned by the software CellAging [29]. We used CellAging to detect RNA-MS2-GFP fluorescence spots (Supplementary Figs. S2B and S2D) and assess the intensity of each spot. From these, integer-valued RNA numbers were calculated for each spot (Supplementary Section I).

Nucleoid(s) segmentation was performed as in [63], using a 2D Gaussian approximation, followed by manual corrections. Cells whose size is smaller than 500 pixels were excluded from the analysis since, in general, they were not real cells (e.g. only half of the cell appeared in the image). Also removed were cells larger than 1000 pixels, as they were abnormally elongated. In general, this led to removing < 5% of the cell population.

The segmentation of the intracellular regions with significant GyrA-YFP was done using a tailored software, SCIP [56]. Errors were manually corrected. To remove measurement noise, we applied a 2D Gaussian filter to each region [94].

2.8. Models and simulations

We use stochastic models of gene expression to test if arrests during elongation, caused by PSB, disturb significantly the mean RNA production rate (within realistic intervals of parameter values).

These models are at single-cell, and single-molecule level. Specifically, two models are simulated. One is the 'Single-Nucleotide

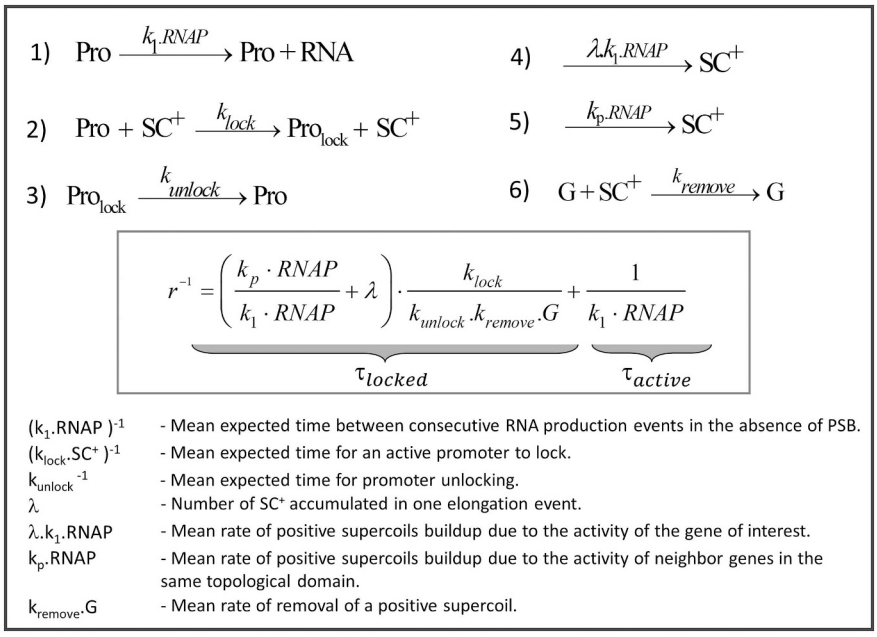

Fig. 1. Minimal (reduced) model of the dynamics of RNA production and transcription locking due to PSB of a chromosome-integrated gene in *E. coli*. The model includes the promoter when active (*Pro*) and when locked due to PSB (Pro_{Lock}), RNA molecules, RNA polymerases (*RNAP*), Gyrases (*G*), and positive supercoils (SC^+). Reaction 1 represents transcription at the rate k_1, which is the basal rate of RNA production of an active promoter assuming one RNAP in the cell. Reaction 2 models promoter locking due to PSB, with k_{lock} being the rate at which an active promoter is locked given the presence of one SC^+. Positive supercoils emerge during transcription of the gene of interest (reaction 4) and/or from the activity of genes in the same topological domain (reaction 5). λ corresponds to a tenth of the number of nucleotides of the gene of interest. Reaction 3 accounts for the unlocking of the promoter at the rate k_{unlock}. Finally, reaction (6) models the removal of positive supercoils by Gyrases. All parameter values are extracted or derived from empirical data , including measurements of a chromosome-integrated $LacO_3O_1$ promoter (k_1 = 0.0014 s^{-1}, k_{lock} = 0.0012 s^{-1} and k_{unlock} = 7 × 10^{-4} s^{-1}) (Supplementary Sections IV and V).

model' (SN Model), since elongation is modelled at the single nucleotide level (Supplementary section II). The other is the "Minimal model', as it is designed from the former, but lacks elongation at the nucleotide level (Fig. 1, Section 3.1).

The time length of each simulation is 10^5 s, found to be long enough for not underestimating the mean length of the time intervals between consecutive RNA production events (which would bias the data with right-censoring) [30]. The simulations have a reading time of 1 s^{-1}. The results shown in the Results section are obtained from 100 runs per condition, as this number suffices to obtain consistent results. Finally, the initials components at the start of simulations are 1 promoter (where the transcription start site is located), 1 Gyrase, and 28 RNAPs. In addition, the SN model has also 4058 nucleotides, in the state "unoccupied" (Supplementary Section II) along which elongation will occur.

The models are implemented in the simulator SGNSim [74] and their dynamics follow the Stochastic Simulation Algorithm [23,24]. In short, the stochastic nature of their dynamics arises from the generation of two random numbers at each step. As described in [24], one of these random numbers determines what is the next reaction (which differs with the propensity of each reaction at that moment), while the other random number determine when the next event will occur (which depends on the total propensity when considering all possible reactions combined). SGNSim makes use of 'Mersenne Twister' to produce these random variables at each step [57].

3. Results

3.1. Expected effects of changing gyrase concentration on the dynamics of transcription

We started by designing a stochastic model of transcription at the single nucleotide level (here named 'SN model'), described in detail in Supplementary Section II and shown in Supplementary Table S2. The model is based on a model proposed in [75] and later used in [53,72], to which we add positive supercoiling buildup/removal. The reactions composing the model should not be interpreted as elementary transitions. Instead, they represent the rates of the rate-limiting steps of the various events. The model dynamics and simulations are described in Materials and Methods, Section 2.8, while its assumption of homogeneous mixing of RNAP and Gyrases is validated in Supplementary Section III.3.

The model consists of the following events (Table S2): transcription starts when an RNAP finds the promoter (reaction S2.1) and unwinds the DNA for reading and escapes the promoter (reaction S2.5). After this, stepwise transcription elongation is initiated, accounting for realistic RNAP footprint in the DNA template, transcriptional pausing, arrests, editing, premature terminations, pyrophosphorolysis and collisions between RNA polymerases [53].

In addition, the model accounts for the phenomenon of production of positive supercoils during elongation [46,51,95], in reaction S2.6 in Supplementary Table S2. As these supercoils accumulate, they enhance the propensity for RNAP arrest (reaction S2.11) [20,51] and transcription initiation locking (reaction S2.2) [9]. The removal of positive supercoils by Gyrase [84] is also modelled explicitly (reaction S2.17). Finally, the model accounts for the potential accumulation of positive supercoils due to transcriptional activity of neighbor genes (reaction S2.4).

This model does not include RNA degradation, as we measured RNA numbers by MS2-GFP tagging, which prevents degradation for a few hours (Supplementary Section I and Figs. S1 and S2) [26,86], thus avoiding this source of noise. Further, for the purposes of this work, we are only interested in RNA production rates, which do not depend on degradation.

Results in Supplementary Sections III.1 and III.2 show that this SN model mimics the effects of PSB on the kinetics of stepwise transcription elongation. Namely, from Supplementary Fig. S6A, one finds that the mean elongation time increases as Gyrase numbers are decreased. Meanwhile, from Supplementary Fig. S6B, one finds that this slowdown of stepwise elongation does not affect the mean rate of RNA production, within the range of parameter values tested, which is expected.

Note that in this model, for the realistic range of parameter values considered, once the system reaches steady state (near constant number of RNAPs on the DNA strand), the mean RNA production rate depends only on the rate with which RNAPs initiate new elongation events (reaction S2.1 in Table S2) and on the rate of abortions of elongation (reaction S2.14 in Table S2), with the latter being near negligible (~4% per transcription initiation event). Only in the unlikely scenario of excessive accumulation of RNAPs in the DNA template that would jam the promoter region, would events in elongation affect the mean RNA production rate.

Therefore, for purposes of estimating the effects of changing Gyrase

concentration on the mean RNA production rate, we instead use a minimal model, where elongation is not explicitly represented. Fig. 1 shows the minimal model that, as the SN model, also has a stochastic dynamics in accordance to the SSA (Materials and Methods, Section 2.8). In detail, reaction 1 models RNA production by an active promoter, *Pro*, and its propensity differs with the basal transcription rate, k_1, and with RNA polymerase numbers. Meanwhile, reaction 2, which models transcription locking, is in all identical to reaction S2.2 of the SN model and, thus, its propensity differs with the number of positive supercoils (Supplementary Section II).

Positive supercoils can be generated via reactions 4 and 5 (also as in the SN model) [1,9,51,70,83,84,89]. The propensity of reaction 4 depends on the basal transcription rate, k_1, of the gene of interest, as described in [17] and in agreement with results from anchored plasmids [9,87] as well as with results reported here. The parameter λ in reaction 4 accounts for the length of the gene of interest (RNAP will take longer to transcribe a longer gene, during which time positive supercoils are produced). As for reaction 5, responsible for the accumulation of PSB due to the transcription activity in the topological domain of the gene of interest, its kinetics differs with the neighboring activity, which can be tuned by k_p and RNAP numbers (Fig. 1).

Once locked, a promoter can become unlocked via reaction 3. The unlocking kinetics can be tuned by the rate constant k_{unlock}. Because the propensity for locking changes linearly with the number of positive supercoils, the propensity for reaction 3 is kept independent from this number. Else, the overall time spent in locked states would change quadratically with the inverse of Gyrase numbers, and not linearly (Fig. 3 provides empirical support for the assumption that this relationship is linear within realistic ranges of parameter values). Finally, reaction 6 represents the removal of positive supercoils by Gyrases. As this takes place, the propensity for reaction 2 decreases, thereby accounting for the expected decrease in the effects of PSB with increasing Gyrase numbers [9].

To verify that the minimal model constitutes a valid approximation of the SN model, we performed simulations for various Gyrase numbers. Visibly, from Supplementary Fig. S6E, the minimal model matches the mean rate of RNA production of the SN model (and the empirical data) as a function of Gyrase numbers. This is expected since, as noted, all its parameter values are the same as in the SN model, except for reaction 4 in Fig. 1, since this reaction needs to account for the number of nucleotides of the gene of interest (which are modelled explicitly in the SN model). This adjustment is done by having the rate of SC^+ production of the gene of interest dependent on its nucleotide length (with λ equaling a tenth of its number of nucleotides, as this is approximately the expected number of SC^+ produced during one elongation event [84]).

We then derived an analytical solution of the minimal model, for the inverse of the mean rate of RNA production (r^{-1}) as a function of Gyrase (inset of Fig. 1). Here, τ_{active} is the mean time between consecutive RNA production events of an unlocked/active promoter, which equals the inverse of $k_1 \times$ RNAP (with RNAP being the number of RNA polymerases). Meanwhile, r is the inverse of the sum of τ_{active} and τ_{locked}, with the latter being the mean time spent in locked states (equation in the larger inset in Fig. 1). From this solution, we find that increasing [G] decreases τ_{locked} [9,46], which increases r. In detail, r^{-1} is expected to change linearly with $[G]^{-1}$ (large inset, Fig. 1). If this holds true, from measurements of r and [G], it should be possible to extrapolate τ_{active}, since τ_{active} should equal r^{-1} for infinite [G]. Further, from τ_{active} and r, it should be possible to estimate τ_{locked}. Finally, note that while k_1 does not affect the mean time for Gyrase to release the gene from a locked state, it does affect the rate of occurrence of locked states.

Interestingly, many plasmids only have weak, transient topological barriers (such as short-term protein-DNA complexes [42]). In particular, aside from when they are anchored to the membrane [3,11,49,71] or have many tandem copies of a DNA-binding site [42], no long-term PSB is expected, since positive and negative supercoils diffuse in opposite directions and annihilate one another [42] (unlike in the chromosome that has topological barriers). As such, it should be possible to simulate the dynamics of plasmid-borne genes using the model in Fig. 1, by setting k_{lock} to null, causing τ_{locked} to be null. Consequently, r^{-1} of a model plasmid-borne gene should equal τ_{active} of the same model gene, when chromosome-integrated. Further, if this holds true, then a plasmid-borne gene can be used as a proxy for the same gene when chromosome-integrated when unaffected by PSB.

3.2. Changing intracellular concentration of gyrases

Above, we hypothesized that r^{-1} should be linear with respect to $[G]^{-1}$ within a given range of Gyrase concentrations (see Fig. 1 and Supplementary Section VI). If true, one should observe a line on a Lineweaver–Burk plot [44] of r^{-1} against $[G]^{-1}$, from which one can extrapolate τ_{active}. From τ_{active} and r, one can then estimate τ_{locked}.

To test this hypothesis, it is necessary to measure r in cells differing in [G]. For this, we inserted a plasmid carrying a copy of the *gyraseA* and *gyraseB* genes under the control of the Rhamnose promoter (pZe11 P_{rham} gyrAB, Materials and Methods). We further added sfGFP, also under the control of the Rhamnose promoter (pZe11 P_{rham} gyrAB-*sfGFP*, Section 2.1 and Supplementary Fig. S4). The region coding for sfGFP allows measuring mRNA coding for Gyrase and the corresponding protein levels produced solely by the plasmid.

We subjected cells to different Rhamnose concentrations until finding a range for which the production rate of the mRNA coding for Gyrase increases linearly with Rhamnose concentration. For this, we performed qPCR using the region of the RNA from the plasmid that is absent in the native RNA coding for Gyrase (i.e. the region coding for sfGFP). In Fig. 2A we find a linear relationship between mRNA fold changes (measured by qPCR) and Rhamnose (0, 0.1, 0.2 and 0.4%). In particular, small deviations from linearity were rejected (p-value > 0.5, see Fig. 2 legend for details).

Next, we verified that cell growth rates were not disturbed in this

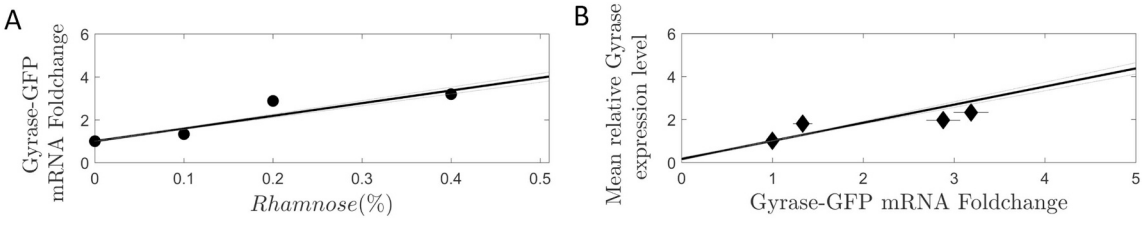

Fig. 2. Gyrase overexpression levels. (A) Fold change of mRNA Gyrase-GFP measured by qPCR, for different concentrations of Rhamnose (0, 0.1, 0.2 and 0.4%), standard error of the mean (vertical error bars) are not visible. Results are relative to the control condition (0% Rhamnose). Also shown is the best-fit line. (B) Calibration line between relative Gyrase-GFP mean expression levels (measured by flow cytometer with the FITC-H detection channel) and mRNA Gyrase-GFP fold change measured by qPCR for 0, 0.1, 0.2 and 0.4% Rhamnose. Gyrase numbers are relative to the 0% Rhamnose condition. Horizontal error bars represent the standard error of the mean. For both figures, we fitted a first order polynomial to the data points by WTLS by minimizing χ^2 [39]. To determine if small deviations from linearity are statistically significant, we performed a likelihood ratio test between the best linear fit and fits by higher order polynomials. In both cases, the test did not reject the linear model (p-values larger than 0.5 and 0.15, for Fig. 2A and B, respectively).

range (Supplementary Fig. S5B). Further, to test if morphology was affected, we measured cell areas in the control condition (165 cells analyzed) and when subject to 0.4% Rhamnose (182 cells analyzed). The cell area was obtained from phase contrast images, using the software iCellFusion (Section 2.7). We performed a 2-sample Kolmogorov-Smirnov test and found that, at the significance level of 0.05, the two distributions cannot be distinguished (p-value of 0.5).

Finally, we verified that, within this range of conditions, the mean relative Gyrase expression level changed linearly with the RNA production rate of the plasmid coding for Gyrase (Fig. 2B), as measured by Flow-cytometry (Section 2.5). In particular, small deviations from linearity were rejected (p-value of 0.15, see Fig. 2 legend for details). We thus conclude that the fold change in Gyrase-GFP protein levels corresponds to the fold change in the mRNA coding for Gyrase-GFP (Supplementary Section VII and Table S3 show the parameters of the calibration line and procedure).

We expect the quantitative relationship between mRNA and protein numbers of the plasmid-borne Gyrase to be the same as in the native Gyrase mRNA and proteins, since we used the native ribosome binding site in the plasmid construct. Thus, we measured by qPCR the fold change of the mRNA produced by both the native and the plasmid-borne Gyrase genes and used the line in Fig. 2B as a calibration line, to estimate the fold change with Rhamnose in Gyrase protein levels (Supplementary Section VII and Table S3).

Finally, we considered that Gyrase overexpression could change the proteome and, eventually, change cellular functioning (e.g. in 1–2 h). To mitigate effects from this eventuality (to avoid unknown changes in the processes represented in Fig. 1), subsequent measurements were conducted 1 h after inducing Gyrase overexpression (Materials and Methods). Given this and the above, we expect that, for 0.2% or lower Rhamnose concentrations (Fig. 2A), changes in RNA production rate in this time window are largely due to changes in concentrations of the components of the reactions in Fig. 1.

3.3. Transcription rate of a chromosome-integrated gene under the control of $P_{LacO3O1}$ in the absence of positive supercoiling buildup

Data in [85] indicates that the expression rate of (at least) three of the RNAP sub-units are, in normal conditions, approximately double the average expression rate of *E. coli* genes. Since several highly expressed genes are supercoiling sensitive [17], it is tangible that Gyrase overexpression may affect [RNAP], which according to the model (Fig. 1), could affect the transcription rate (r) of our gene of interest (Fig. 1). Thus, we first assessed for potential fast changes in [RNAP] when overexpressing Gyrase.

For this, we used the same plasmid as above, with the *gyrA* and *gyrB* genes controlled by a Rhamnose promoter, to overexpress Gyrase (but having removed sfGFP, so as to not affect RNA counting or Gyrase functioning, see Materials and Methods). Next, we measured [RNAP] at the different Rhamnose concentrations (0%, 0.1% and 0.2%) by measuring the RpoC protein by Western blot, 1 h after inducing Gyrase overexpression. From Fig. 3A and B, at the same OD_{600}, the [RNAP] differs by 12% between the two extreme conditions. This difference was found to be statistically significant by a 1-sample 2-tailed t-test, with the null hypothesis that the increase is 12% (p-value of 0.42). In addition, we performed a 2-sample, 2-tailed t-test with the null hypothesis that there is no difference between the conditions, which was rejected (p-value of 0.0008). This is expected to partially explain changes in r due to Gyrase overexpression and, thus, needs to be accounted for when quantifying the direct effects of changing [G] (Supplementary Section VIII).

In addition, it is tangible that overexpression of Gyrase could affect the negative supercoiling state of the chromosome, e.g. by introducing negative supercoils [6,47,80]. This, in turn, could affect DNA supercoiling density and its folding and compaction [36,92], which could alter transcription rates by affecting the time-lengths of open complex formations [52].

Unfortunately, we cannot measure directly the *in vivo* kinetics of open complex formation at a given Gyrase concentration, as this would require measuring the *in vivo* transcription in cells with differing RNAP concentrations [48,81], which would also affect the intracellular Gyrase concentration. Therefore, instead, we estimated indirectly if Gyrase overexpression (between 0% and 0.2% Rhamnose) suffices to alter significantly the chromosome folding and compaction. For this, we assessed if the nucleoid area (with area being a proxy for compaction strength) is altered by Gyrase overexpression, using DAPI staining and image analysis (Sections 2.2 and 2.7).

The mean and standard deviation of the nucleoid area, when and when not overexpressing Gyrase, are shown in Table S4. We performed a 2-sample student t-test for the null hypothesis that the two data sets of absolute nucleoid area come from the same distribution. The test did not reject the null-hypothesis (p-value > 0.01). We thus conclude that, in the range of Gyrase overexpression levels used here, the nucleoid size was not significantly affected. As such, we do not expect the indirect effects of Gyrase overexpression on DNA supercoiling density to significantly affect the kinetics of open complex formation.

Given this, we again used the plasmid with the *gyrA* and *gyrB* genes controlled by a Rhamnose promoter (without sfGFP) to study the effects of Gyrase overexpression on transcription initiation locking due to PSB of a chromosome-integrated gene under the control of $P_{LacO3O1}$. This promoter was used as its dynamics has been previously studied when plasmid-borne, including using single-RNA MS2-GFP tagging [34,54,64,66,81].

We first measured the absolute mean r^{-1} in the control condition (Materials and Methods, Section 2.3) by microscopy measurements of integer valued RNA numbers in single cells at different time moments (Supplementary Section IX). The absolute mean r^{-1} in the control condition was found to equal 1476 s, with a standard error of 145 s.

Using the value of r^{-1} in the control condition, we scaled the relative qPCR values to obtain the values of r^{-1} in conditions where Gyrase is overexpressed. Results from qPCR are shown in Supplementary Table S1. In these, the gradually increasing expression of Gyrase did not affect significantly the expression of the 16S rRNA gene. This is expected, since 16S rRNA is a stable component of ribosomes and, thus, should not change significantly between conditions when growth rates are not affected significantly [88] (Supplementary Fig. S5B). Namely, even if the small changes between conditions were considered significant, there is no monotonic change with increasing Rhamnose concentration. As such, 16S rRNA is used as the reference gene.

Next, from Supplementary Table S1 and the microscopy data in the control condition, we obtained absolute rates of RNA production in each condition (black circles in Fig. 3C). Finally, we fitted a line by weighted total least squares (WTLS) [39] (black line in Fig. 3C) to estimate τ_{active} (where the line intersects the Y-axis), when not accounting for changes in [RNAP]. We performed a likelihood ratio test between the best linear fit and fits of higher order polynomials which showed that the linear model best fits the data (p-value > 0.9).

Next, from the [RNAP] in each condition (Fig. 3B) and the model fitting (Supplementary Section IV), we estimated the effects of changes in [RNAP] (Supplementary Section VIII and Supplementary Table S5). Supplementary Figs. S7A and S7B show the Z surfaces of the best fitting models and empirical results. From the R^2 values (legend of Supplementary Fig. S7), one finds that the model well-fits the empirical data. We thus used this model to estimate the weight of the changes in [RNAP] (Fig. 3B) on r^{-1} and then quantified the changes in r^{-1} due to changes in [G] alone. Results are shown in the blue circles in Fig. 3C. Next, we fitted a line (blue line in Fig. 3C) to these data points using WTLS, from which we estimated r^{-1} for infinite [G] (i.e. τ_{active}) to be 749 ± 247 s.

Finally, we determined if the small deviations from linearity are statistically significant by performing a likelihood ratio test between

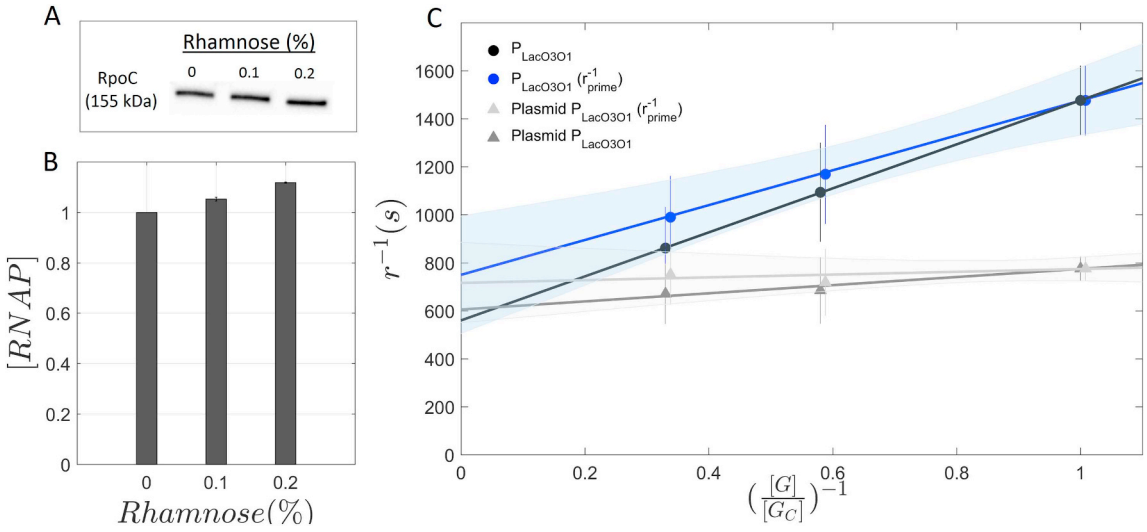

Fig. 3. Effects of Gyrase overexpression in the RNA production rate of $LacO_3O_1$ when chromosome-integrated and when plasmid-borne. (A) Replicate of Western Blot image of RpoC subunit for cells subjected to 0, 0.1% and 0.2% Rhamnose. (B) Bar chart of [RNAP] fold change with Gyrase overexpression, relative to the control condition (0% Rhamnose). In all conditions, OD_{600} was 0.6. (C) LineWeaver-Burk plot of the inverse of the RNA production rate (r^{-1}), for different Gyrase concentrations (black circles), relative to the control ($[G]/[G_C] = 1$) of the chromosome-integrated construct. Also shown is the standard error of the mean (vertical error bars), along with the best-fit line (black line). Further shown are the RNA production rates after correcting for the weight of the changes in [RNAP] (r^{-1}_{prime}), when overexpressing Gyrase (blue circles) and the correspondent best-fit line (blue solid line) and its standard error of the mean (light blue area) obtained by Monte Carlo simulations (5000 iterations). Blue circles are 0.008 units deviated to the right, for figure legibility. The equations of the black and blue lines are $r^{-1} = (917 \pm 329) \times \left(\frac{[G]}{[G_C]}\right)^{-1} + (559 \pm 246)$ and $r^{-1} = (726 \pm 329) \times \left(\frac{[G]}{[G_C]}\right)^{-1} + (749 \pm 247)$, respectively. Finally, the dark grey triangles are the values of r^{-1} for the plasmid-borne construct, when subject to the same levels of Gyrase overexpression while the light grey triangles correspond to r^{-1} after correcting for the weight of the changes in [RNAP] on r^{-1} (dark grey triangles). Light grey triangles are 0.008 units deviated to the right, for figure legibility. Also shown are the respective best-fit lines and its standard errors of the mean (light grey area) obtained by Monte Carlo simulations (5000 iterations). The equation of the dark grey line is $r^{-1} = (168 \pm 184) \times \left(\frac{[G]}{[G_C]}\right)^{-1} + (605 \pm 167)$. The equation of the light grey line is $r^{-1} = (58 \pm 184) \times \left(\frac{[G]}{[G_C]}\right)^{-1} + (715 \pm 167)$. Data from 368 cells (chromosome-integrated gene) and 476 cells (plasmid-borne gene). (For interpretation of the references to colour in this figure legend, the reader is referred to the web version of this article.)

the best linear fit and fits by higher order polynomials (by WTLS by minimizing χ^2) [39]. The test did not reject the linear model (p-value > 0.9), from which we conclude that r^{-1} decreases linearly with $[G]^{-1}$.

Several phenomena could have forced this plot to be non-linear. E.g., if the ratio between free and total Gyrase concentrations would increase as Gyrase is overexpressed, the plot would exhibit negative curvature (see Section VI in Supplementary). Meanwhile, if the resolution of supercoils in the control condition was near-saturation, overexpressing Gyrase would result in positive curvature. We therefore interpret the observed linearity as evidence that these changes in r^{-1} are largely due to changes in [RNAP] and [G] as assumed by the model in Fig. 1, rather than due to unknown factors.

3.4. Transcription kinetics of $P_{LacO3O1}$ when single-copy plasmid-borne

To validate the estimation of τ_{active}, we integrated the same gene under the control of $P_{LacO3O1}$ into a single-copy plasmid (Materials and Methods). We expect this to reduce the effects of PSB on the activity of the gene of interest to a minimum. I.e., the value of r^{-1} of the single copy plasmid-borne gene should approximate the estimated τ_{active} of the chromosome-integrated gene. If this holds true, adding Novobiocin, which inhibits Gyrase activity [9,15,22,91], should not disturb significantly its activity.

To test this, we performed time-lapse microscopy measurements of RNA numbers in cells subject to 100 μg/ml Novobiocin (Materials and Methods). Images were taken every 15 min, starting 30 min after introducing 1 mM IPTG in the media to ensure full induction of the target gene [86]. We also performed measurements where Novobiocin was not added.

From Supplementary Fig. S4B, the RNA production rate of the plasmid-borne gene is not affected by the addition of Novobiocin, as expected if PSB is absent. Meanwhile, in the absence of Novobiocin, we observe the same behavior but higher r, which is consistent with the cells subject to Novobiocin having lesser number of active RNAP and/or σ factors [8,13,18,76], etc. Further, both behaviors are significantly different from cells with the chromosome-integrated construct subject to Novobiocin, where a clear blocking of the RNA production is observed shortly after adding Novobiocin (Fig. 4, blue line). We conclude that the gene in the single-copy plasmid is not directly affected by Novobiocin, suggesting that it is impervious to the effects from PSB.

In support, according to the model (Fig. 1), for equal mean RNA production rate, the kinetics of RNA production from a gene unaffected by PSB (such as when on a single-copy plasmid) should be less noisy than otherwise (e.g. when chromosome-integrated) [64]. Lesser noise should reduce cell-to-cell variability in RNA numbers. To test this, we compared the squared coefficient of variation of RNA numbers in single cells, CV^2(RNA), in conditions where the two constructs exhibit the same mean RNA numbers per cell (50 μM IPTG for the plasmid-borne gene and 1000 μM IPTG for the chromosome-integrated gene, Supplementary Fig. S4A). The CV^2(RNA) in cells with the chromosome-integrated construct is found to be much higher than in cells with the single-copy plasmid-borne gene (3.18 and 1.58, respectively), in agreement with the model prediction, even though the plasmid-borne gene is being partially affected by LacI repression, which adds variability in RNA numbers [48].

Finally, we verified that the RNA production rate of the single-copy plasmid construct equals the inverse of τ_{active} of the chromosome construct. For this, we performed microscopy measurements of the integer valued RNA numbers in cells with the plasmid construct and estimated r^{-1} to be 775 ± 50 s (dark grey triangle in Fig. 3C, for the control condition). This result cannot be distinguished, in a statistical sense,

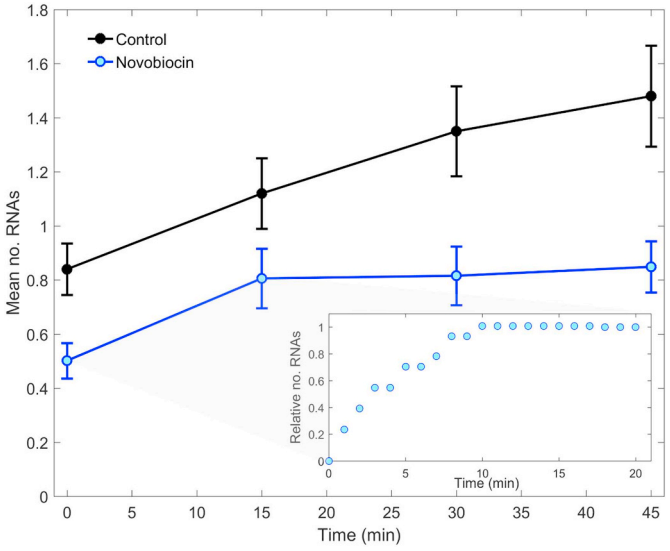

Fig. 4. RNA production over time. Mean integer-valued RNA numbers in individual cells with the chromosome-integrated $P_{LacO3O1}$ when subjected to 100 μg/ml Novobiocin (blue line) and in the control condition (black line, absent of Novobiocin). Measurements performed by microscopy, with single RNA tagging by MS2-GFP. For each time point, new cells were taken from the original culture. On average, 200 cells were used per condition. Error bars represent the standard error of the mean. Finally, the inset shows the number of RNA production events per cell relative to the total number of RNAs produced during the measurement time. Data collected at the single RNA level, from time-lapse microscopy measurements with images taken once per minute. (For interpretation of the references to colour in this figure legend, the reader is referred to the web version of this article.)

from the estimate of τ_{active} for the chromosome construct assuming infinite [G] (749 ± 247 s) (in agreement with the model predictions, Fig. 1).

In this regard, in Supplementary Section X, we estimated the minimum PSB effects that would be detectable, provided the same degree of sensitivity in the measurements of r^{-1}. We found that there needs to exist a fold change between two conditions of, at least, 1.6. However, we estimate that tripling the number of data points collected allows a reduction of this number to 1.2.

Further, we also performed qPCR measurements of the plasmid construct when subject to the same levels of Gyrase overexpression. Results are shown in Fig. 3C. Next, we fitted a line (dark grey line in Fig. 3C) to the data points. From this, we find that the change in RNA production rate of the plasmid gene with gyrase overexpression is ~5 times weaker than in the chromosome-integrated construct. Next, using WTLS [39] we tested if the small deviations from linearity are statistically significant. The test did not reject the linear model (p-value > 0.8). Subsequently, as before, we corrected the data points to account for the changes in RNAP concentrations. Results in Fig. 3 (light grey line) show that the corrected line is nearly horizontal and, as expected, cannot be distinguished from a horizontal line, in a statistically sense, using the same test as above. We conclude that the RNA production kinetics from the plasmid construct is nearly non-responsive to Gyrase overexpression.

In this regard, note that estimation of τ_{active} when accounting for changes in [RNAP] (blue line in Fig. 3C) fits the measurements better (light grey line in Fig. 3C), then when not accounting for [RNAP] changes (black line in Fig. 3C). From comparing the blue and black circles in each condition, we also find that, e.g., for maximum Gyrase (0.2% Rhamnose), the increase in [RNAP] accounts for 31% of the decrease in r^{-1} relative to the control, with the remaining 69% being due to increased [G] (and/or other, unknown factors). Similarly, in the extrapolated condition of infinite [G], the increase in [RNAP], compared to the control condition, accounts for 41% of the decrease in r^{-1}, with the remaining 59% being due to increased [G].

3.5. Mean time spent in locked states and average number of transcription events between consecutive locking events

Since Fig. 3 shows that r^{-1} changes linearly with $[G]^{-1}$, we used the Lineweaver-Burk equation [44] to estimate the mean time spent in locked states, τ_{locked}, as follows:

$$\tau_{locked} = \frac{[G]_2(r_2^{-1} - r_1^{-1})}{([G]_1 - [G]_2)} \quad (1)$$

From (1), given the control and the condition where relative $[G]^{-1}$ is 0.33 (0% and 0.2% Rhamnose, respectively), we infer τ_{locked} to be 735 s, with a standard error of the mean (SEM) of 341 s (obtained by the Delta Method [5]). Using the other pair of conditions (0% and 0.1% Rhamnose) we obtain the same result, in a statistical sense. As the mean time interval between transcription events is 1476 s, we estimate transcription initiation locking due to PSB to account for ~50% of this interval.

Meanwhile, to estimate the mean number of transcription events between consecutive locked states, N, consider that, according to the model:

$$N = \frac{\tau_{escape}}{\tau_{locked}} \quad (2)$$

To solve for N, we used the value of τ_{locked} obtained above, and τ_{escape} obtained from measurements in [9], which reported that the average DNA binding time of Gyrase is ~333 s while the unbind time is $\sim 10^3$ s [9]. Since Gyrase is expected to resolve multiple positive supercoils during this time [1,84], we assumed that the sum of these times (~1333 s) is an upper bound of the time for a locked gene to escape PSB (i.e. τ_{escape}). Introducing the estimated values of τ_{locked} and τ_{escape} in eq. 2, we find that N equals ~1.8 ± 0.84.

3.6. Kinetics of transcription initiation locking in the presence of a gyrase inhibitor

To validate the above estimations, we performed time series measurements at the single-RNA level in cells carrying the chromosome-integrated $P_{LacO3O1}$ subject to Novobiocin, a Gyrase inhibitor [22]. Assuming that, when Novobiocin first enters the cytoplasm, $P_{LacO3O1}$ activity is not subject to PSB, then the mean number of RNAs produced until transcription ceases should correspond to the mean number of transcription events between consecutive locking events. As it is not likely that the gene of interest is absent of effects from PSB in all cells, the empirical result should correspond to a lower bound estimate. Interestingly, from the same experiment, it should also be possible to measure τ_{active} (Fig. 1) from the time for RNA production to cease in all cells.

First, we tested whether Novobiocin, at the concentrations used here, affects cell morphology. For this, as above, we measured cell areas in the control condition (165 cells analyzed) and when subject to 100 ng /ml Novobiocin (180 cells analyzed), and then performed a 2-sample Kolmogorov-Smirnov test. We found that, at the significance level of 0.05, the two distributions cannot be distinguished (p-value of 0.13).

Next, we measured integer-valued number of RNAs in individual cells over time, every 15 min, 45 min after inducing the target gene (with IPTG) and adding Novobiocin (Gyrase inhibitor), so as to account for the mean time taken by cells to intake IPTG [64,86] and because only at this moment did we observe any tangible reduction in transcription activity (inset in Fig. 4). RNAs were detected by MS2-GFP tagging, preventing RNA degradation (Materials and Methods). We also performed a control experiment, where Novobiocin was not introduced.

Results in Fig. 4 show that when and only when adding Novobiocin,

the RNA production ceases. In the presence of Novobiocin, on average we observed 0.8 ± 0.11 RNAs per cell after 15 min. Considering mean cell division times (Fig. S5), we estimated the mean number of RNAs produced per cell for 15 min to be ~1.04 ± 0.14. This agrees (statistically) with the above estimation of N (~1.8 ± 0.84). It also agrees with past estimations that, in live cells, transcription initiation locking can occur after less than 5 transcription events [9].

We also extracted the time for transcription events to cease after introducing Novobiocin. For this, we performed additional time-lapse microscopy (1 min interval between images). The number of RNAs produced in individual cells during the observation time were obtained as in (66) and verified by visual inspection. Results in the inset of Fig. 4 show that transcription activity started to be reduced at minute 1 and that no RNA was produced after 10 min, which can be used as a lower bound for τ_{active} (see above). This agrees with the previous estimation of τ_{active} (~12 ± 4 min) from Fig. 3.

3.7. Effects of PSB differ with the basal transcription rate

Previous works reported evidence that a gene's activity affects its own PSB when the gene is on a circular template tethered to a surface [9,87]. We hypothesized that the same occurs on a chromosome-integrated gene, due to discrete topological constraints. This follows from the reasoning that, if the expected time interval between consecutive transcription events becomes longer, while [G] is kept constant, there is more time for Gyrase to resolve transcription initiation locking due to PSB in between transcription events. The model in Fig. 1 accounts for this, as the responsiveness of r^{-1} to changes in [G] should decrease with k_1. To test this, we replaced $P_{LacO3O1}$ by a native Lac promoter (P_{Lac}). We chose this promoter because it has similar sequence and repression-activation mechanism (Methods), which could affect PSB, and because it exhibits slower RNA production when fully induced (Supplementary Fig. S4A). By being in the same location, we expect the contribution to PSB from the activity of neighboring genes to be the same.

First, we obtained an induction curve of P_{Lac} (Supplementary Fig. S4A). Visibly, under maximum induction, P_{Lac} has a slower transcription rate than $P_{LacO3O1}$ (less ~62% MS2-GFP tagged RNAs per cell). In detail, r^{-1} (P_{Lac}) equals 2704 ± 493 s (obtained as described in Supplementary Section IX).

Next, we measured by qPCR the transcription rate for various [G] (as in Fig. 3). Results were scaled by r^{-1} in the control condition (Fig. 5A, black diamonds). Afterwards, we fitted a line by WTLS (black line in Fig. 5A) and corrected its slope by accounting for changes in [RNAP] (Supplementary Section VIII). Finally, we fitted a (green) line by WTLS to the corrected data points (green diamonds in Fig. 5A). From the best fitting (green) line in Fig. 5A we find that, for maximum [G] (0.2% Rhamnose), the increase in [RNAP] explains 28% of the increase in r, with the remaining 72% being due to increased [G] and/or unknown factors.

To assess if the effects of PSB differ with the promoter strength, we plotted r^{-1} against $([G]/[G_C])^{-1}$ for both constructs (P_{Lac} and $P_{LacO3O1}$). Results in Fig. 5B show that r^{-1} decreases faster with [G] for $P_{LacO3O1}$ (in agreement with the model). We thus conclude that changing [G] has smaller effects in the effective transcription rate of the lesser active promoter (P_{Lac}).

3.8. Inference of the parameter values of the model that best fit the empirical data and prediction of τ_{locked} as a function of the basal transcription rate

We searched for parameter values for the model (Fig. 1) that best match the empirical data of both $P_{LacO3O1}$ and P_{Lac}, assuming that they differ only in the basal transcription rate (k_1). We found that the model fits the empirical data with a mean squared error of 0.0004 and R^2 values larger than 0.95 (Supplementary Figs. S7A and S7B).

From the fitting, we obtained the parameter values (α, β_1, β_2, and η, Supplementary Section V) and inferred the duty cycles of transcription initiation locking due to neighboring and 'self-produced' PSB, for each [G] (Table S6). From Table S6, the lower are [G] and τ_{active}, the longer will the gene remain locked and the higher is its OFF/ON duty cycle ratio.

In addition, we used the inferred values of α, β_1, β_2, and η, to extrapolate τ_{locked} relative to r^{-1} as a function of $\frac{[G]}{[G_C]}$ and $\frac{1}{k_1 \times [RNAP]}$. The inferred surface is shown in Fig. 6.

If the differences in the locking dynamics due to PSB of $P_{LacO3O1}$ and P_{Lac} are solely due to the difference in their values of k_1, as hypothesized, this surface should fit other empirical values of $\frac{1}{k_1 \times [RNAP]}$ and $\frac{\tau_{Locked}}{r^{-1}}$ obtained when changing k_1 (e.g. by tuning their induction strength).

We thus performed qPCR measurements when inducing $P_{LacO3O1}$ with 0 and 50 μM IPTG (from Supplementary Fig. S4A, note that, at these concentrations, the number of RNAs produced differs significantly from maximum induction). The results from qPCR measurements, added to Fig. 6, fit well the predicted surface, suggesting that combining data from a promoter(s) of differing basal transcription rates in the same location in the DNA one can predict a state space of possible kinetics of transcription initiation locking of genes differing in k_1 in a given chromosomal location.

4. Discussion and conclusions

Past studies have shown that DNA topology and gene expression mutually affect one another [4,14,37,38].

We found that, for a certain range of Gyrase concentrations, the inverse of the transcription rate of a chromosome-integrated gene controlled by $LacO_3O_1$ changes linearly with the inverse of Gyrase concentration, while not perturbing cell growth or morphology. Given this, we developed and validated a method that uses a LineWeaver-Burk plot to dissect, from single-cell, single-RNA data, key kinetic parameters of transcription initiation locking due to PSB. Namely, we dissected the rate of occurrence of these locks and their weight on the effective RNA production rate. Next, we compared with a promoter at the same chromosomal location and similar in structure and regulation but differing in strength. From this, we inferred a range of potential kinetics of transcription initiation locking in a given topological domain that can be achieved by tuning the basal transcriptional rate of the gene of interest. Relevantly, the method was sensitive to detect PSB effects causing a minimum of 1.6 fold changes in transcription rates. Further, we estimate that simple enhancements (e.g. increasing the number of data points used for the LineWeaver-Burk plot from 3 to 10) reduced this to 1.2 fold changes. Other improvements (e.g. higher precision in data collection) should further enhance the sensitivity, which should suffice to, e.g., dissect the effects of interference between closely spaced promoters (Supplementary Section X).

To an extent, the interpretation of the empirical data relies on the models and, thus, it is necessary to assess their reliability, i.e. the robustness of their predictions. In this regard, we observed that, first, the models accurately estimated how much of the change in r^{-1}, following Gyrase overexpression, is due to changes in RNAP numbers (Fig. 3). In detail, the dynamics of the chromosome integrated gene, when corrected for RNAP changes (with this correction relying on the model), only differs from the plasmid dynamics by 3.5% (not statistically significant) while, prior to considering the model, it differed by 28%. Second, the model predicted the mean time to lock the promoter due to PSB (τ_{active} ~12 min) from qPCR and population level microscopy data. This estimation was validated by direct measurements using time-lapse microscopy data at the single cell level (one image per minute). In detail, estimated and real data differed solely by ~15% that, when accounting for the measurement error, is also not statistically significant (Figs. 3 and 4). Further, the model accurately predicted (in a statistical sense) how much the basal transcription rate affects the

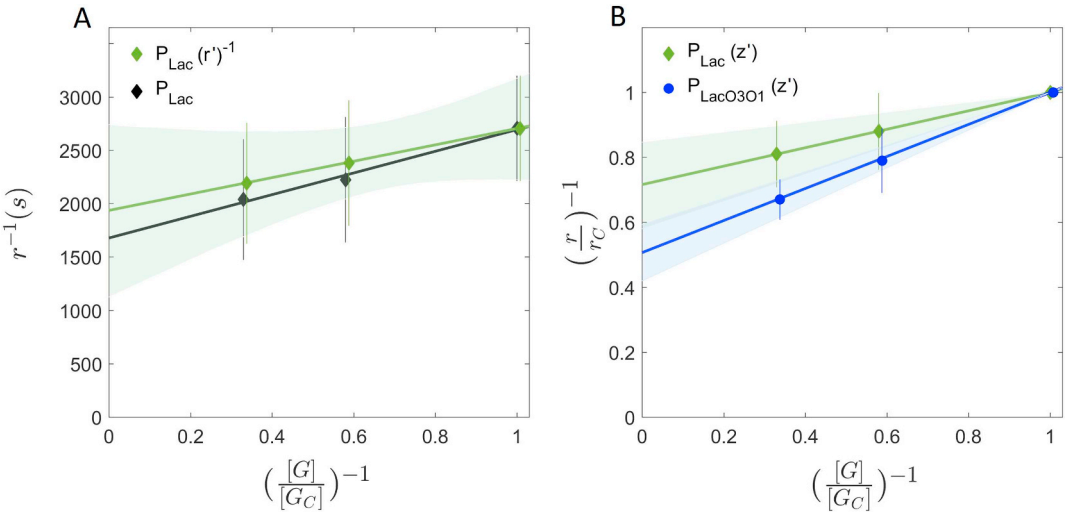

Fig. 5. LineWeaver-Burk plots for P_{Lac} and $P_{LacO3O1}$. (A) LineWeaver-Burk plot of the inverse of the RNA production rate of the chromosome-integrated Lac gene for different Gyrase concentrations (black diamonds), relative to the control (0% Rhamnose). Also shown are the standard error of the mean (vertical error bars), along with the best-fit line (black line). Further shown are the inverse of the RNA production rates corrected for the increased RNAP concentration when overexpressing Gyrase (r'^{-1}), and the correspondent best-fit line (green line) and its standard error of the mean (light green area) obtained by Monte Carlo simulations (10,000 iterations). The green diamonds are 0.008 units deviated to the right, for figure legibility. The line equations are $r^{-1} = (768 \pm 1096) \times \left(\frac{[G]}{[G_C]}\right)^{-1} + (1936 \pm 802)$ and $r^{-1} = (1016 \pm 1096) \times \left(\frac{[G]}{[G_C]}\right)^{-1} + (1677 \pm 802)$ for the green and black lines, respectively. RNA production rates were obtained by qPCR and microscopy. (B) LineWeaver-Burk plot of the inverse of the fold change in RNA production rate of the chromosome-integrated gene under the control of $LacO_3O_1$ (blue circles) and of the chromosome-integrated under the control of Lac gene (green diamonds) against the inverse of the Gyrase concentrations (0, 0.1 and 0.2% Rhamnose induction), measured by qPCR, relative to the control condition (0% Rhamnose). Vertical error bars represent the standard error of the mean. In addition, shown are the best-fit lines and their standard errors of the mean (green and light blue areas), obtained by Monte Carlo simulations (500 iterations). Both lines (blue and green) were corrected for the effects of the RNAP increase in the RNA production rate when overexpressing Gyrase. z' stands for the ratio $\left(\frac{r}{r_C}\right)^{-1}$ after the correction. The blue circles are 0.008 units deviated to the right, for legibility. The line equations are $\left(\frac{r}{r_C}\right)^{-1} = (0.28 \pm 0.13) \times \left(\frac{[G]}{[G_C]}\right)^{-1} + (0.72 \pm 0.13)$ and for the green and blue lines, respectively. (For interpretation of the references to colour in this figure legend, the reader is referred to the web version of this article.)

fraction of time spent by the promoter in locked state (Fig. 6). Finally, the estimations of k_1 and k_{unlock} using the models agree with past estimations (respectively in [9,48]).

Overall, the results suggest that the weight of PSB on the effective RNA production rate of a gene depends not only on the mean activity of the DNA loop that the gene belongs to, but also on the basal transcription activity of the observed gene. This dependence was found to be sufficiently strong to require the introduction of this phenomenon in the model, if one is to predict the effects of changing Gyrase levels on the dynamics of transcription (reaction 4 in Fig. 1). This is because the fraction of time spent in locked states depends not only on the rate of accumulation of positive supercoils, but also on how much time Gyrases have to resolve enough supercoils (in between consecutive transcription events) to avoid reaching a supercoiling density that suffices for promoter locking.

Given that increasing the *basal* transcription rates enhances the influence of PSB on the *effective* transcription rate, we hypothesize that, at least in some genes, increasing the basal transcription rate may come at the cost of increased transcriptional noise due to PSB, even if lowering the noise from basal transcription dynamics. We thus expect that the relationship between basal transcription rate and PSB needs to be directly accounted for in models of prokaryotic gene expression. As such, when reducing the SN model (Supplementary Table S2) to a minimal model (Fig. 1), one of the critical components kept from the SN model was reaction 4 (Fig. 1), as it is responsible for the production positive supercoils at a rate that differs with the basal transcription rate of the gene interest.

This was required even though, similar to past models [4,9], there is also reaction 5, which introduces positive supercoils from 'external' sources, at a rate that differs with the average transcriptional activity of all genes in the same DNA loop (or topological domain) [17,43] and DNA replication [84]. Interestingly, the existence of this dependency suggests that it should be possible to, some extent, regulate the robustness of chromosome-integrated synthetic circuits to PSB, by tuning its own transcription rates, as well as placing it in a topological domain with desired mean activity.

In this regard, since increasing the basal transcription rate enhances the effects of PSB, is there an effective upper limit on the transcription rate? If so, this could potentially explain (at least partially) why some genes exist in multi-copy form. Such form would allow crossing this limit, while also supporting more stable expression levels.

Meanwhile, the combination of the results from two different constructs suggest that it may be possible to map a state space of transcription initiation locking of the topological domains of *E. coli*. However, since domain barriers are not likely to be at fixed sites [45,70,92], it may be necessary to set constructs in various regions of the DNA and measure not only the mean, but also the variability of the propensity for transcription locking as a function of DNA location. Using several constructs, differing in features (e.g. in regulatory mechanisms), should allow accounting for changes in parameters, other than the basal transcription rate. Namely, while here we mapped a 1-dimensional space by tuning the basal transcription rate, changing other variables would facilitate mapping a multi-dimensional state-space of transcription initiation locking kinetics. We expect such mapping to be of use in dissecting global transcription programs of *E. coli*, as well as for implementing chromosome-integrated synthetic circuits with predictable kinetics.

Our methodology may also assist in quantifying effects of environmental shifts (e.g. temperature) on the kinetics of transcription initiation locking. One could then explore whether *E. coli* uses this

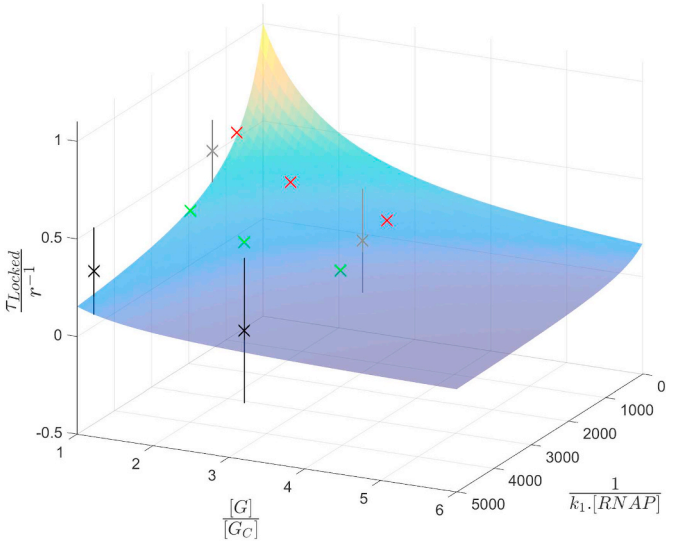

Fig. 6. Expected time in locked states relative to the expected interval between consecutive RNA production events as a function of Gyrase concentration and of the inverse of the basal transcription rate ($k_1{}^{-1}$), with $\tau_{active} = \frac{1}{k_1.[RNAP]}$. The surface is the model prediction of the relative τ_{Locked} as a function of τ_{active} and of the Gyrase concentration relative to the control. Red crosses are the empirical data for the $LacO_3O_1$ promoter under full induction (1000 μM IPTG), green crosses are the empirical data for the native Lac promoter under full induction (1000 μM IPTG), grey crosses are the empirical data for the $LacO_3O_1$ promoter under 50 μM IPTG induction, and black crosses are the empirical data for the $LacO_3O_1$ promoter uninduced (0 μM IPTG). The vertical bars are the standard error of the mean. All error bars intersect the surface. (For interpretation of the references to colour in this figure legend, the reader is referred to the web version of this article.)

phenomenon to adapt to fluctuating environments. This hypothesis is supported by recent observations [64] that cold-shock genes have atypical supercoiling-sensitivity (for unknown reasons). I.e., genes with long-term responses to cold-shocks appear to be impervious to supercoiling, while genes with short-term responses have more-than-expected-by-chance sensitivity to supercoiling. Our methodology may assist in dissecting the responsible mechanisms, e.g. by measuring τ_{locked} and τ_{active} of these genes following mutations, etc.

We expect our methodology to be compatible with other techniques. E.g., it is potentially valuable to combine it with measurements of local DNA supercoiling density, such as trimethylpsoralen intercalation [40], to quantify the relationship between this density and the effects of PSB on transcription. Similarly, it may be valuable to combine it with the method in [48] to dissect the kinetics of rate limiting steps of active transcription initiation. For chromosome-integrated genes, we expect that only by using both methods will be possible to estimate the times spent prior to open complex formation, since models suggest that this state of activity will differ with the kinetics of promoter locking due to PSB [59], due to the expected competition between the formations of closed complexes and locked states.

Further, our methodology should be applicable using other techniques, such as RNA FISH (Fluorescence in situ hybridization) [79] and RNA aptamer-fluorogen systems [12,19,65,82,98].

Finally, our results derived from a first attempt at dissecting the *in vivo* dynamics of locking of transcription initiation using a Lineweaver-Burk plot. Many questions remain unanswered and require further study. It may turn out that fluctuations in Gyrase concentration have non-uniform effects at the genome-wide level, due to the dependency on basal transcription rates and mean rates of topological domains. Potentially, this could be used by cells as means to activate specific gene cohorts (e.g. of genes sharing the same topological domain), involved in responsive transcriptional programs. It could also be used to change the state of small genetic circuits responsible for triggering response programs to fluctuations in supercoiling density (e.g. fluctuations in supercoiling densities may alter the stable state of a, e.g., genetic switch with genes in different topological domains). If this holds true, the 'optimal' level of Gyrase may differ with the environment and/or internal cell state, depending on whether a given gene cohort (supercoiling density dependent) should be active or not.

In conclusion, the methods and results here presented are expected to support near-future research on the role of Gyrase on the global dynamics of gene regulatory networks.

Funding

This work was supported by the Finnish Academy of Science and Letters [to C.P.]; Pirkanmaa Regional Fund [to V.K.]; Tampere University Graduate Program (Finland) [to V.C. and M.B.]; EDUFI Fellowship [TM-19-11105 to S.D.]; Academy of Finland [295027 to A.S.R.]; and Jane and Aatos Erkko Foundation [610536 to A.S.R.]. The funders had no role in study design, data collection and analysis, decision to publish, or preparation of the manuscript.

Author's statement

C.P. and A.S.R. conceived the study. C.P. performed data analysis. C.P., M.B., and A.S.R. performed modelling. V.K.K., M.M., V.C., and S.D. performed measurements. C.P., V.K., and A.S.R. drafted the manuscript, which was revised by all authors. The authors declare no competing interests.

Transparency document

The Transparency document associated this article can be found, in online version.

Declaration of competing interest

The authors declare that they have no conflict of interest.

Appendix A. Supplementary data

Supplementary data to this article can be found online at https://doi.org/10.1016/j.bbagrm.2020.194515.

References

[1] R.E. Ashley, A. Dittmore, S.A. McPherson, C.L. Turnbough, K.C. Neuman, N. Osheroff, Activities of gyrase and topoisomerase IV on positively supercoiled DNA, Nucleic Acids Res. 45 (16) (2017) 9611–9624, https://doi.org/10.1093/nar/gkx649.
[2] N. Blot, R. Mavathur, M. Geertz, A. Travers, G. Muskhelishvili, Homeostatic regulation of supercoiling sensitivity coordinates transcription of the bacterial genome, EMBO Rep. 7 (7) (2006) 710–715, https://doi.org/10.1038/sj.embor.7400729.
[3] J.D. Boeke, P. Model, A prokaryotic membrane anchor sequence: carboxyl terminus of bacteriophage f1 gene III protein retains it in the membrane, Proc. Natl. Acad. Sci. U. S. A. 79 (17) (1982) 5200, https://doi.org/10.1073/pnas.79.17.5200.
[4] C.H. Bohrer, E. Roberts, A biophysical model of supercoiling dependent transcription predicts a structural aspect to gene regulation, BMC Biophys. 9 (1) (2015) 2, https://doi.org/10.1186/s13628-016-0027-0.
[5] G. Casella, R.L. Berger, Statistical Inference, Thomson Learning, 2002.
[6] J.J. Champoux, DNA topoisomerases: structure, function, and mechanism, Annu. Rev. Biochem. 70 (1) (2001) 369–413, https://doi.org/10.1146/annurev.biochem.70.1.369.
[7] B. Cheng, C.-X. Zhu, C. Ji, A. Ahumada, Y.-C. Tse-Dinh, Direct interaction between *Escherichia coli* RNA polymerase and the zinc ribbon domains of DNA topoisomerase I, J. Biol. Chem. 278 (33) (2003) 30705–30710, https://doi.org/10.1074/jbc.M303403200.
[8] B.-K. Cho, D. Kim, E.M. Knight, K. Zengler, B.O. Palsson, Genome-scale reconstruction of the sigma factor network in *Escherichia coli*: topology and functional states, BMC Biol. 12 (1) (2014) 4, https://doi.org/10.1186/1741-7007-12-4.
[9] S. Chong, C. Chen, H. Ge, X.S. Xie, Mechanism of transcriptional bursting in Bacteria, Cell 158 (2) (2014) 314–326, https://doi.org/10.1016/j.cell.2014.05.038.
[10] K.A. Datsenko, B.L. Wanner, One-step inactivation of chromosomal genes in

Escherichia coli K-12 using PCR products, Proc. Natl. Acad. Sci. 97 (12) (2000) 6640–6645, https://doi.org/10.1073/pnas.120163297.
[11] S. Deng, R.A. Stein, N.P. Higgins, Organization of supercoil domains and their reorganization by transcription, Mol. Microbiol. 57 (6) (2005) 1511–1521, https://doi.org/10.1111/j.1365-2958.2005.04796.x.
[12] E.V. Dolgosheina, S.C.Y. Jeng, S.S.S. Panchapakesan, R. Cojocaru, P.S.K. Chen, P.D. Wilson, N. Hawkins, P.A. Wiggins, P.J. Unrau, RNA mango aptamer-fluorophore: a bright, high-affinity complex for RNA labeling and tracking, ACS Chem. Biol. 9 (10) (2014) 2412–2420, https://doi.org/10.1021/cb500499x.
[13] T. Dong, H.E. Schellhorn, Global effect of RpoS on gene expression in pathogenic *Escherichia coli* O157:H7 strain EDL933, BMC Genomics 10 (1) (2009) 349, https://doi.org/10.1186/1471-2164-10-349.
[14] C.J. Dorman, M.J. Dorman, DNA supercoiling is a fundamental regulatory principle in the control of bacterial gene expression, Biophys. Rev. 8 (S1) (2016) 89–100, https://doi.org/10.1007/s12551-016-0238-2.
[15] K. Drlica, Control of bacterial DNA supercoiling, Mol. Microbiol. 6 (4) (1992) 425–433, https://doi.org/10.1111/j.1365-2958.1992.tb01486.x.
[16] M. Drolet, Growth inhibition mediated by excess negative supercoiling: the interplay between transcription elongation, R-loop formation and DNA topology, Mol. Microbiol. 59 (2006) 723–730, https://doi.org/10.1111/j.1365-2958.2005.05006.x.
[17] D. El Hanafi, L. Bossi, Activation and silencing of leu-500 promoter by transcription-induced DNA supercoiling in the Salmonella chromosome, Mol. Microbiol. 37 (3) (2000) 583–594, https://doi.org/10.1046/j.1365-2958.2000.02015.x.
[18] A. Farewell, K. Kvint, T. Nyström, Negative regulation by RpoS: a case of sigma factor competition, Mol. Microbiol. 29 (4) (1998) 1039–1051, https://doi.org/10.1046/j.1365-2958.1998.00990.x.
[19] G.S. Filonov, J.D. Moon, N. Svensen, S.R. Jaffrey, Broccoli: rapid selection of an RNA mimic of green fluorescent protein by fluorescence-based selection and directed evolution, J. Am. Chem. Soc. 136 (46) (2014) 16299–16308, https://doi.org/10.1021/ja508478x.
[20] K. Fujita, M. Iwaki, T. Yanagida, Transcriptional bursting is intrinsically caused by interplay between RNA polymerases on DNA, Nat. Commun. 7 (2016) 13788, , https://doi.org/10.1038/ncomms13788.
[21] G. Fulcrand, S. Dages, X. Zhi, P. Chapagain, B.S. Gerstman, D. Dunlap, F. Leng, DNA supercoiling, a critical signal regulating the basal expression of the lac operon in *Escherichia coli*, Sci. Rep. 6 (1) (2016) 19243, , https://doi.org/10.1038/srep19243.
[22] M. Gellert, M.H. O'Dea, T. Itoh, J. Tomizawa, Novobiocin and coumermycin inhibit DNA supercoiling catalyzed by DNA gyrase, Proc. Natl. Acad. Sci. U. S. A. 73 (12) (1976) 4474–4478, https://doi.org/10.1073/pnas.73.12.4474.
[23] D.T. Gillespie, A general method for numerically simulating the stochastic time evolution of coupled chemical reactions, J. Comput. Phys. 22 (4) (1976) 403–434, https://doi.org/10.1016/0021-9991(76)90041-3.
[24] D.T. Gillespie, Exact stochastic simulation of coupled chemical reactions, J. Phys. Chem. 81 (1977) 2340–2361, https://doi.org/10.1021/j100540a008.
[25] I. Golding, E.C. Cox, RNA dynamics in live *Escherichia coli* cells, Proc. Natl. Acad. Sci. U. S. A. 101 (31) (2004) 11310–11315, https://doi.org/10.1073/pnas.0404443101.
[26] I. Golding, J. Paulsson, S.M. Zawilski, E.C. Cox, Real-time kinetics of gene activity in individual bacteria, Cell 123 (6) (2005) 1025–1036, https://doi.org/10.1016/j.cell.2005.09.031.
[27] N.S.M. Goncalves, S.M.D. Oliveira, V. Kandavalli, J.M. Fonseca, A.S. Ribeiro, Temperature dependence of leakiness of transcription repression mechanisms of *E. coli*, Lect. Notes Comput. Sci 9859 (2016) 341–342.
[28] P. Guptasarma, Cooperative relaxation of supercoils and periodic transcriptional initiation within polymerase batteries, BioEssays 18 (4) (1996) 325–332, https://doi.org/10.1002/bies.950180411.
[29] A. Hakkinen, A.-B. Muthukrishnan, A. Mora, J.M. Fonseca, A.S. Ribeiro, CellAging: a tool to study segregation and partitioning in division in cell lineages of *Escherichia coli*, Bioinformatics 29 (13) (2013) 1708–1709, https://doi.org/10.1093/bioinformatics/btt194.
[30] A. Häkkinen, A.S. Ribeiro, Characterizing rate limiting steps in transcription from RNA production times in live cells, Bioinformatics 32 (9) (2016) 1346–1352, https://doi.org/10.1093/bioinformatics/btv744.
[31] C.D. Hardy, N.R. Cozzarelli, Alteration of *Escherichia coli* topoisomerase IV to novobiocin resistance. *Antimicrob*, Agents Chemother. 47 (3) (2003) 941–947, https://doi.org/10.1128/aac.47.3.941-947.2003.
[32] Y. Hayakawa, T. Murotsu, K. Matsubara, Mini-F protein that binds to a unique region for partition of mini-F plasmid DNA, J. Bacteriol. 163 (1) (1985) 349–354.
[33] N.P. Higgins, Species-specific supercoil dynamics of the bacterial nucleoid, Biophys. Rev. 8 (S1) (2016) 113–121, https://doi.org/10.1007/s12551-016-0207-9.
[34] V.K. Kandavalli, H. Tran, A.S. Ribeiro, Effects of σ factor competition are promoter initiation kinetics dependent, Biochim. Biophys. Acta - Gene Regul. Mech. 1859 (10) (2016) 1281–1288, https://doi.org/10.1016/j.bbagrm.2016.07.011.
[35] K. Kirkegaard, J.C. Wang, Bacterial DNA topoisomerase I can relax positively supercoiled DNA containing a single-stranded loop, J. Mol. Biol. 185 (3) (1985) 625–637, https://doi.org/10.1016/0022-2836(85)90075-0.
[36] N. Kleckner, J.K. Fisher, M. Stouf, M.A. White, D. Bates, G. Witz, The bacterial nucleoid: nature, dynamics and sister segregation, Curr. Opin. Microbiol. 22 (2014) 127–137, https://doi.org/10.1016/j.mib.2014.10.001.
[37] M.V. Kotlajich, D.R. Hron, B.A. Boudreau, Z. Sun, Y.L. Lyubchenko, R. Landick, Bridged filaments of histone-like nucleoid structuring protein pause RNA polymerase and aid termination in bacteria, Elife 4 (2015), https://doi.org/10.7554/eLife.04970.
[38] F. Kouzine, S. Sanford, Z. Elisha-Feil, D. Levens, The functional response of upstream DNA to dynamic supercoiling *in vivo*, Nat. Struct. Mol. Biol. 15 (2) (2008) 146–154, https://doi.org/10.1038/nsmb.1372.
[39] M. Krystek, M. Anton, A weighted total least-squares algorithm for fitting a straight line, Meas. Sci. Technol. 18 (11) (2007) 3438–3442, https://doi.org/10.1088/0957-0233/18/11/025.
[40] A. Lal, A. Dhar, A. Trostel, F. Kouzine, A.S.N. Seshasayee, S. Adhya, Genome scale patterns of supercoiling in a bacterial chromosome, Nat. Commun. 7 (1) (2016) 11055, , https://doi.org/10.1038/ncomms11055.
[41] T.B.K. Le, M.V. Imakaev, L.A. Mirny, M.T. Laub, High-resolution mapping of the spatial organization of a bacterial chromosome, Science 342 (6159) (2013) 731–734, https://doi.org/10.1126/science.1242059.
[42] F. Leng, B. Chen, D.D. Dunlap, Dividing a supercoiled DNA molecule into two independent topological domains, Proc. Natl. Acad. Sci. 108 (50) (2011) 19973–19978, https://doi.org/10.1073/pnas.1109854108.
[43] D.M. Lilley, C.F. Higgins, Local DNA topology and gene expression: the case of the leu-500 promoter, Mol. Microbiol. 5 (4) (1991) 779–783, https://doi.org/10.1111/j.1365-2958.1991.tb00749.x.
[44] H. Lineweaver, D. Burk, The determination of enzyme dissociation constants, J. Am. Chem. Soc. 56 (3) (1934) 658–666, https://doi.org/10.1021/ja01318a036.
[45] V.S. Lioy, A. Cournac, M. Marbouty, S. Duigou, J. Mozziconacci, O. Espéli, F. Boccard, R. Koszul, Multiscale structuring of the *E. coli* chromosome by nucleoid-associated and condensin proteins, Cell 172 (4) (2018) 771–783.e18, https://doi.org/10.1016/j.cell.2017.12.027.
[46] L.F. Liu, J.C. Wang, Supercoiling of the DNA template during transcription, Proc. Natl. Acad. Sci. U. S. A. 84 (20) (1987) 7024–7027, https://doi.org/10.1073/pnas.84.20.7024.
[47] Y. Liu, A.M. Berrido, Z.-C. Hua, Y.-C. Tse-Dinh, F. Leng, Biochemical and biophysical properties of positively supercoiled DNA, Biophys. Chem. 230 (2017) 68–73, https://doi.org/10.1016/j.bpc.2017.08.008.
[48] J. Lloyd-Price, S. Startceva, V. Kandavalli, J.G. Chandraseelan, N. Goncalves, S.M.D. Oliveira, A. Häkkinen, A.S. Ribeiro, Dissecting the stochastic transcription initiation process in live *Escherichia coli*, DNA Res. 23 (3) (2016) 203–214, https://doi.org/10.1093/dnares/dsw009.
[49] A.S. Lynch, J.C. Wang, Anchoring of DNA to the bacterial cytoplasmic membrane through cotranscriptional synthesis of polypeptides encoding membrane proteins or proteins for export: a mechanism of plasmid hypernegative supercoiling in mutants deficient in DNA topoisomerase I, J. Bacteriol. 175 (6) (1993) 1645, https://doi.org/10.1128/jb.175.6.1645-1655.1993.
[50] D. Ma, D.N. Cook, M. Alberti, N.G. Pon, H. Nikaido, J.E. Hearst, Genes acrA and acrB encode a stress-induced efflux system of *Escherichia coli*, Mol. Microbiol. 16 (1) (1995) 45–55, https://doi.org/10.1111/j.1365-2958.1995.tb02390.x.
[51] J. Ma, L. Bai, M.D. Wang, Transcription under torsion, Science 340 (6140) (2013) 1580–1583, https://doi.org/10.1126/science.1235441.
[52] J. Ma, M.D. Wang, DNA supercoiling during transcription, Biophys. Rev. 8 (Suppl. 1) (2016) 75–87, https://doi.org/10.1007/s12551-016-0215-9.
[53] J. Mäkelä, J. Lloyd-Price, O. Yli-Harja, A.S. Ribeiro, Stochastic sequence-level model of coupled transcription and translation in prokaryotes, BMC Bioinformatics 12 (1) (2011) 121, https://doi.org/10.1186/1471-2105-12-121.
[54] J. Mäkelä, V. Kandavalli, A.S. Ribeiro, Rate-limiting steps in transcription dictate sensitivity to variability in cellular components, Sci. Rep. 7 (1) (2017) 10588, , https://doi.org/10.1038/s41598-017-11257-2.
[55] H. Mannerstrom, O. Yli-Harja, A.S. Ribeiro, Inference of kinetic parameters of delayed stochastic models of gene expression using a markov chain approximation, EURASIP J. Bioinform. Syst. Biol. 2011 (1) (2011) 572876, , https://doi.org/10.1155/2011/572876.
[56] L. Martins, R. Neeli-Venkata, S.M.D. Oliveira, A. Häkkinen, A.S. Ribeiro, J.M. Fonseca, SCIP: a single-cell image processor toolbox, Bioinformatics (Oxford, England) 34 (24) (2018) 4318–4320, https://doi.org/10.1093/bioinformatics/bty505.
[57] M. Matsumoto, T. Nishimura, Mersenne Twister, ACM Trans. on Modeling and Comp. Simulation 8 (1998) 3–30, https://doi.org/10.1145/272991.272995.
[58] W.R. McClure, Mechanism and control of transcription initiation in prokaryotes, Annu. Rev. Biochem. 54 (1) (1985) 171–204, https://doi.org/10.1146/annurev.bi.54.070185.001131.
[59] N. Mitarai, I.B. Dodd, M.T. Crooks, K. Sneppen, The generation of promoter-mediated transcriptional noise in Bacteria, PLoS Comput. Biol. 4 (7) (2008) e1000109, , https://doi.org/10.1371/journal.pcbi.1000109.
[60] H. Mori, A. Kondo, A. Ohshima, T. Ogura, S. Hiraga, Structure and function of the F plasmid genes essential for partitioning, J. Mol. Biol. 192 (1) (1986) 1–15, https://doi.org/10.1016/0022-2836(86)90459-6.
[61] K. Nevo-Dinur, A. Nussbaum-Shochat, S. Ben-Yehuda, O. Amster-Choder, Translation-independent localization of mRNA in *E. coli*, Science 331 (6020) (2011) 1081–1084, https://doi.org/10.1126/science.1195691.
[62] S. Oehler, M. Amouyal, P. Kolkhof, B. von Wilcken-Bergmann, B. Müller-Hill, Quality and position of the three lac operators of *E. coli* define efficiency of repression, EMBO J. 13 (14) (1994) 3348–3355.
[63] S.M.D. Oliveira, R. Neeli-Venkata, N.S.M. Goncalves, J.A. Santinha, L. Martins, H. Tran, J. Mäkelä, A. Gupta, M. Barandas, A. Häkkinen, J. Lloyd-Price, J.M. Fonseca, A.S. Ribeiro, Increased cytoplasm viscosity hampers aggregate polar segregation in Escherichia coli, Mol. Microbiol. 99 (4) (2016) 686–699, https://doi.org/10.1111/mmi.13257.
[64] S.M.D. Oliveira, N.S.M. Goncalves, V.K. Kandavalli, L. Martins, R. Neeli-Venkata, J. Reyelt, J.M. Fonseca, J. Lloyd-Price, H. Kranz, A.S. Ribeiro, Chromosome and plasmid-borne PLacO3O1 promoters differ in sensitivity to critically low temperatures, Sci. Rep. 9 (1) (2019) 4486, https://doi.org/10.1038/s41598-019-39618-z.
[65] J.S. Paige, K.Y. Wu, S.R. Jaffrey, RNA mimics of green fluorescent protein, Science 333 (6042) (2011) 642–646, https://doi.org/10.1126/science.1207339.

[66] C.S.D. Palma, S. Startceva, R. Neeli-Venkata, M. Zare, N.S.M. Goncalves, J.M. Fonseca, S.M.D. Oliveira, A.S. Ribeiro, A strategy for dissecting the kinetics of transcription repression mechanisms, Proceedings of the European Medical and Biolgical Engineering Conference (EMBEC), June 11–15, Tampere, Finland, 65 Springer, Singapore, 2017, pp. 1097–1100, , https://doi.org/10.1007/978-981-10-5122-7_274 Also published in: IFMBE Proceedings.
[67] D.S. Peabody, The RNA binding site of bacteriophage MS2 coat protein, EMBO J. 12 (2) (1993) 595.
[68] D.S. Peabody, Role of the coat protein-RNA interaction in the life cycle of bacteriophage MS2, Mol. Gen. Genet. MGG 254 (4) (1997) 358–364, https://doi.org/10.1007/s004380050427.
[69] B.J. Peter, J. Arsuaga, A.M. Breier, A.B. Khodursky, P.O. Brown, N.R. Cozzarelli, Genomic transcriptional response to loss of chromosomal supercoiling in *Escherichia coli*, Genome Biol. 5 (11) (2004) R87, https://doi.org/10.1186/gb-2004-5-11-r87.
[70] L. Postow, C.D. Hardy, J. Arsuaga, N.R. Cozzarelli, Topological domain structure of the *Escherichia coli* chromosome, Genes Dev. 18 (14) (2004) 1766–1779, https://doi.org/10.1101/gad.1207504.
[71] G.J. Pruss, K. Drlica, Topoisomerase I mutants: the gene on pBR322 that encodes resistance to tetracycline affects plasmid DNA supercoiling, Proc. Natl. Acad. Sci. U. S. A. 83 (23) (1986) 8952–8956, https://doi.org/10.1073/pnas.83.23.8952.
[72] T. Rajala, A. Häkkinen, S. Healy, O. Yli-Harja, A.S. Ribeiro, Effects of transcriptional pausing on gene expression dynamics, PLoS Comput. Biol. 6 (3) (2010) 29–30, https://doi.org/10.1371/journal.pcbi.1000704.
[73] A. Revyakin, R.H. Ebright, T.R. Strick, Promoter unwinding and promoter clearance by RNA polymerase: detection by single-molecule DNA nanomanipulation, Proc. Natl. Acad. Sci. 101 (14) (2004) 4776–4780, https://doi.org/10.1073/pnas.0307241101.
[74] A.S. Ribeiro, J. Lloyd-Price, SGN Sim, a stochastic genetic networks simulator, Bioinformatics 23 (6) (2007) 777–779, https://doi.org/10.1093/bioinformatics/btm004.
[75] A.S. Ribeiro, O.-P. Smolander, T. Rajala, A. Häkkinen, O. Yli-Harja, Delayed stochastic model of transcription at the single nucleotide level, J. Comput. Biol. 16 (4) (2009) 539–553, https://doi.org/10.1089/cmb.2008.0153.
[76] P.E. Rouvière, A. De Las Peñas, J. Mecsas, C.Z. Lu, K.E. Rudd, C.A. Gross, rpoE, the gene encoding the second heat-shock sigma factor, sigma E, in *Escherichia coli*, EMBO J. 14 (5) (1995) 1032–1042.
[77] N. Rovinskiy, A.A. Agbleke, O. Chesnokova, Z. Pang, N.P. Higgins, Rates of gyrase supercoiling and transcription elongation control supercoil density in a bacterial chromosome, PLoS Genet. 8 (8) (2012) e1002845, , https://doi.org/10.1371/journal.pgen.1002845.
[78] J. Santinha, L. Martins, A. Häkkinen, J. Lloyd-Price, S.M.D. Oliveira, A. Gupta, T. Annila, A. Mora, A.S. Ribeiro, J.R. Fonseca, iCellFusion: Tool for Fusion and Analysis of Live-Cell Images from Time-Lapse Multimodal Microscopy, (2016), https://doi.org/10.4018/978-1-4666-8811-7.ch004.
[79] R.H. Singer, D.C. Ward, Actin gene expression visualized in chicken muscle tissue culture by using in situ hybridization with a biotinated nucleotide analog, Proc. Natl. Acad. Sci. U. S. A. 79 (23) (1982) 7331–7335, https://doi.org/10.1073/pnas.79.23.7331.
[80] C. Sissi, M. Palumbo, In front of and behind the replication fork: bacterial type IIA topoisomerases, Cell. Mol. Life Sci. 67 (12) (2010) 2001–2024, https://doi.org/10.1007/s00018-010-0299-5.
[81] S. Startceva, V.K. Kandavalli, A. Visa, A.S. Ribeiro, Regulation of asymmetries in the kinetics and protein numbers of bacterial gene expression, Biochim. Biophys. Acta - Gene Regul. Mech. 1862 (2) (2019) 119–128, https://doi.org/10.1016/j.bbagrm.2018.12.005.
[82] R.L. Strack, M.D. Disney, S.R. Jaffrey, A superfolding Spinach2 reveals the dynamic nature of trinucleotide repeat–containing RNA, Nat. Methods 10 (12) (2013) 1219–1224, https://doi.org/10.1038/nmeth.2701.
[83] M. Stracy, C. Lesterlin, F. Garza de Leon, S. Uphoff, P. Zawadzki, A.N. Kapanidis, Live-cell superresolution microscopy reveals the organization of RNA polymerase in the bacterial nucleoid, Proc. Natl. Acad. Sci. 112 (32) (2015) E4390–E4399, https://doi.org/10.1073/pnas.1507592112.
[84] M. Stracy, A.J.M. Wollman, E. Kaja, J. Gapinski, J.-E. Lee, V.A. Leek, S.J. McKie, L.A. Mitchenall, A. Maxwell, D.J. Sherratt, M.C. Leake, P. Zawadzki, Single-molecule imaging of DNA gyrase activity in living *Escherichia coli*, Nucleic Acids Res. 47 (1) (2019) 210–220, https://doi.org/10.1093/nar/gky1143.
[85] Y. Taniguchi, P.J. Choi, G.W. Li, H. Chen, M. Babu, J. Hearn, A. Emili, X.S. Xie, Quantifying *E. coli* proteome and transcriptome with single-molecule sensitivity in single cells, Sci. (New York, NY) 329 (5991) (2010) 533–538, https://doi.org/10.1126/science.1188308.
[86] H. Tran, S.M.D. Oliveira, N. Goncalves, A.S. Ribeiro, Kinetics of the cellular intake of a gene expression inducer at high concentrations, Mol. BioSyst. 11 (9) (2015) 2579–2587, https://doi.org/10.1039/C5MB00244C.
[87] Y.P. Tsao, H.Y. Wu, L.F. Liu, Transcription-driven supercoiling of DNA: direct biochemical evidence from in vitro studies, Cell 56 (1) (1989) 111–118, https://doi.org/10.1016/0092-8674(89)90989-6.
[88] T. Větrovský, P. Baldrian, The variability of the 16S rRNA gene in bacterial genomes and its consequences for bacterial community analyses, PLoS One 8 (2) (2013) e57923, , https://doi.org/10.1371/journal.pone.0057923.
[89] S.M. Vos, E.M. Tretter, B.H. Schmidt, J.M. Berger, All tangled up: how cells direct, manage and exploit topoisomerase function, Nat. Rev. Mol. Cell Biol. 12 (12) (2011) 827–841, https://doi.org/10.1038/nrm3228.
[90] J.C. Wang, DNA topoisomerases, Annu. Rev. Biochem. 54 (1) (1985) 665–697, https://doi.org/10.1146/annurev.bi.54.070185.003313.
[91] James C. Wang, DNA Topoisomerases, Annu. Rev. Biochem. 65 (1) (1996) 635–692, https://doi.org/10.1146/annurev.bi.65.070196.003223.
[92] X. Wang, P.M. Llopis, D.Z. Rudner, Organization and segregation of bacterial chromosomes, Nat. Rev. Genet. 14 (3) (2013) 191–203, https://doi.org/10.1038/nrg3375.
[93] A. Wegerer, T. Sun, J. Altenbuchner, Optimization of an *E. coli* L-rhamnose-inducible expression vector: test of various genetic module combinations, BMC Biotechnol. 8 (1) (2008) 2, https://doi.org/10.1186/1472-6750-8-2.
[94] A. Wheeler, Digital Microscopy, in: A. Wheeler, R. Henriques (Eds.), Standard and Super-Resolution Bioimaging Data Analysis, 2017, https://doi.org/10.1002/9781119096948.ch1.
[95] H.Y. Wu, S.H. Shyy, J.C. Wang, L.F. Liu, Transcription generates positively and negatively supercoiled domains in the template, Cell 53 (3) (1988) 433–440, https://doi.org/10.1016/0092-8674(88)90163-8.
[96] E. Yeung, A.J. Dy, K.B. Martin, A.H. Ng, D. Del Vecchio, J.L. Beck, J.J. Collins, R.M. Murray, Biophysical constraints arising from compositional context in synthetic gene networks, Cell Syst 5 (1) (2017) 11–24.e12, https://doi.org/10.1016/j.cels.2017.06.001.
[97] E.L. Zechiedrich, A.B. Khodursky, S. Bachellier, R. Schneider, D. Chen, D.M.J. Lilley, N.R. Cozzarelli, Roles of topoisomerases in maintaining steady-state DNA supercoiling in Escherichia coli, J. Biol. Chem. 275 (11) (2000) 8103–8113, https://doi.org/10.1074/jbc.275.11.8103.
[98] J. Zhang, J. Fei, B.J. Leslie, K.Y. Han, T.E. Kuhlman, T. Ha, Tandem spinach array for mRNA imaging in living bacterial cells, Sci. Rep. 5 (1) (2015) 17295, , https://doi.org/10.1038/srep17295.
[99] R. Samul, F. Leng, Transcription-coupled Hypernegative Supercoiling of Plasmid DNA by T7 RNA Polymerase in Escherichia coli Topoisomerase I-Deficient Strains, Journal of Molecular Biology 374 (4) (2007) 925–935, https://doi.org/10.1016/j.jmb.2007.10.011.